A Comparison of Single-Point, Multi-Point and Range-Based Objectives for Transonic Aerofoil Optimization

D.J. Poole [*], C.B. Allen [†], T.C.S. Rendall[‡]

Department of Aerospace Engineering, University of Bristol, Bristol, BS8 1TR, U.K.

The most common aerofoil optimization problem considered is lift-constrained drag minimization at a fixed design point, however, shock-free solutions can result which can lead to poor off-design performance. As such, this paper presents a study into the construction of the aerofoil optimization problem and its effect of the performance over a range of operating conditions. Single- and multi-point optimizations of aerofoils in transonic flow are considered and an improved range-based optimization problem subject to a constraint on fixed non-dimensional wing loading with a varying design point is formulated. This problem is more representative of the aircraft design problem though similar in cost to single-point drag minimization. An analytical treatment using an approximation of wave drag is also presented which demonstrates that the optimum Mach number for a fixed shape is supercritical if the required loading is above a critical threshold. Optimizations are presented that show that to define an effective objective function, three-dimensional effects modelled via an induced drag term must be introduced. The general trend is to produce solutions with higher Mach numbers and lower lift coefficients, and that shocked solutions perform better when considering the performance in range over the operating space. Furthermore, the resulting aerofoil shapes are supercritical in nature; a particularly promising result.

Nomenclature

a, b	Linear surface pressure coefficient approximation constants

[*]Senior Teaching Associate. Email: d.j.poole@bristol.ac.uk

[†]Professor of Computational Aerodynamics. Email: c.b.allen@bristol.ac.uk

[‡]Lecturer. Email: thomas.rendall@bristol.ac.uk

AR	Aspect ratio
C_L	Lift coefficient
$C_{L_{incomp}}$	Incompressible lift coefficient
C_D	Drag coefficient
C_{D_w}	Wave drag coefficient
C_{D_0}	Non-wave drag coefficient
C_P	Surface pressure coefficient
$C_{P_{min}}$	Minimum surface pressure coefficient
C_P^*	Critical pressure coefficient
D	Drag
f	Modified Prandtl-Glauert correction
g	Prandtl-Glauert correction
F	Range-optimal polynomial function
J	Objective function
k	Lock calibration constant
k_1, p_1, M_0	Modified Prandtl-Glauert correction calibration constants
l	Non-dimensional wing loading ($M^2 C_L$)
L	Lift
M ($\equiv M_\infty$)	Freestream Mach number
M_c	Critical Mach number
M_{dd}	Drag divergent Mach number
M_{opt}	Range-optimal Mach number
n	Number of design variables
N	Number of design points
r	Breguet range
R	Breguet range parameter
R_κ	Breguet range parameter with induced drag correction
Re	Reynolds number
t	Optimizer iteration counter
V	Volume
x, y, z	Inertial coordinates
$\mathbf{X}^{new}, \mathbf{X}^{old}$	Deformation and undeformed aerofoil shape
κ	Induced drag coefficient ($1/\pi AR$)

$\mathbf{g}$	Inequality constraint vector
$\mathbf{h}$	Equality constraint vector
$\mathbf{U}$	Modal deformation matrix
$\mathbf{U}'$	Truncated (first n columns) modal deformation matrix
$\mathbf{V}$	Modal weighting matrix
$\boldsymbol{\alpha}$	Design variable vector
$\boldsymbol{\lambda}$	Design point weighting vector
$\boldsymbol{\Delta X}$	Training data deformation matrix ($2N \times m_{def}$)
$\boldsymbol{\Sigma}$	Modal energy diagonal matrix

I. Introduction and Background

Aerodynamic shape optimization (ASO) is the process used to optimize aerodynamic shapes within a computational environment to improve on design requirements. Numerical simulation methods to model fluid flows are used routinely in industrial design, and increasing computer power has resulted in their integration into the optimization process to produce the ASO framework. The aerodynamic model (normally a computational fluid dynamics (CFD) flow solver) is used to evaluate some metric against which to optimize, which in the case of ASO is an aerodynamic quantity, most commonly drag, subject to a set of constraints which are usually aerodynamic or geometric in nature. Along with the fluid flow model, the ASO framework requires a surface parameterization scheme, which mathematically describes the aerodynamic shape being optimized by a series of design variables. Numerous advanced optimizations using compressible computational fluid dynamics (CFD) as the aerodynamic model have previously been performed [1–5], and the authors have presented work in this area, having developed a modularised, generic optimization tool, that is flow solver and mesh type independent, and applicable to any aerodynamic problem [6, 7].

Aerodynamic drag reduction is a commonly-studied optimization problem. For typical cruising conditions of a modern transport aircraft, the flow is transonic, often resulting in a shock; this causes wave drag and also affects the boundary layer. Eliminating the shock therefore leads to large reductions in the drag of the section and, in inviscid flow, should theoretically lead to a zero drag section. In the first two of a trilogy of papers, Morawetz [8, 9] proved that shock-free solutions in inviscid transonic flow around aerofoils were isolated. Due to this result, it was considered difficult, if not impossible, to obtain a shock-free aerofoil design. However, the hodograph method [10] allowed shock-free designs to be achieved [11, 12]. Harbeck and Jameson [13] later quantified the front in the Mach-C_L space between where shock-free solutions were and were not able

to be obtained. Nowadays, shock-free designs for transonic flows around aerofoils are commonly obtained; for example, of the benchmark cases from the AIAA Aerodynamic Design and Optimization Discussion Group (ADODG) [a] shock-free results are readily available for case 2 (transonic, viscous, drag minimization of RAE2822) [14–18], and a low drag solution has recently been published for case 1 (inviscid, non-lifting, drag minimization of NACA0012) by the authors[19].

The goal of point design, that can lead to shock-free solutions, is the substantial performance improvement at the design point. However, the off-design performance is often severely compromised, and may be much worse than the initial solution. It was proved in the final paper of the trilogy by Morawetz [20] that shock-free aerofoils in transonic flow would have a shock if the freestream Mach number was perturbed. The flow structure for these types of aerofoils tends to be a single shock for an increase in the freestream Mach number and a double shock for a decrease in the Mach number [21]. Hence, using a single-point design for aerofoil optimization can be problematic. This issue was also considered when designing the NASA supercritical aerofoils; Harris [22] stated *"permitting a weak shock rather than trying to design for a shock-free design point also reduces the off-design penalties usually associated with point design airfoils"*.

A common way of dealing with the off-design problems is to use multi-point design, where the objective is a combination of the objective at different design points. The idea is to reach a compromised solution which, while not being optimal at a number of discrete design points, is a trade-off of the performance at those design points, which leads to lower off-design penalties. Many examples of multi-point design can be found in the literature, see, for example [4, 23, 24], or the AIAA ADODG case 4 results [17, 25, 26].

Two common issues tend to arise when applying multipoint optimization. The first is that to apply it successfully requires careful selection of both the design points (these are often known *a priori* but can be determined using gradient span analysis [27]), and the weightings between the objectives at those design points. This issue can be eased by using automated weight selections [28, 29], an integral approach [30] or a probabilistic approach [31]. The second common issue is the cost surrounding multi-point optimization. By the nature of the problem, multipoint design requires a flow solution at each design point per objective function evaluation. This makes performing high-fidelity, multi-point optimization on fine numerical grids prohibitively expensive for more than a handful of design points.

Further issues with multi-point optimization were highlighted in a comprehensive study by Drela [32]. Drela considered single-, two- and four-point optimizations and hypothesised that to avoid point design at each of the considered design points, the number of chosen operating points should be of the order of the number of design variables (this was later validated from a mathematical argument [33]). The problem tends to go back to the proven theory of Morawetz, where, unless there is a shocked solution, a shock will result for a deviation in freestream Mach number, even if multiple points are considered. Hence, the problem of

[a] https://info.aiaa.org/tac/ASG/APATC/AeroDesignOpt-DG/default.aspx

posing a suitable transonic aerofoil optimization problem is still an open one [17, 34].

An alternative approach to the construction of the aerodynamic optimization problem, including the choice of design point, design variables, objective function and constraints is considered here alongside the conventional single- and multi-point drag minimization problem. Maximization of the Breguet range parameter, ML/D, is considered, subject to constant non-dimensional wing loading (see section III for more details on how this is formulated). This design problem is not often studied in aerodynamic optimization, however, examples of it can be found in historical aircraft design. For example, figure 1 (which was constructed using the data in the book of Mair and Birdsall [35][b], which itself is a processed form of the data from Hanke and Nordwall [36]) shows the range parameter variation with Mach number for different non-dimensional wing loadings of early variants of the Boeing 747.

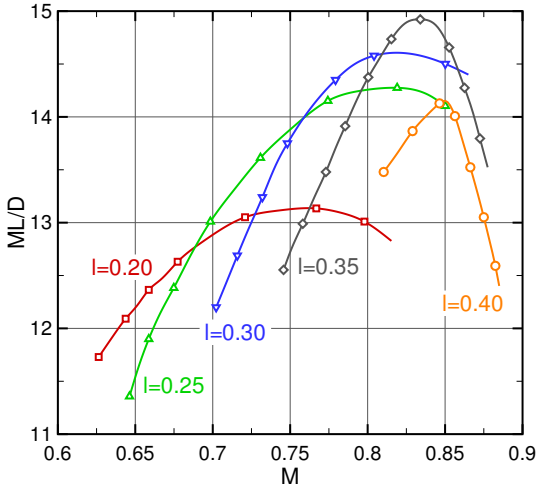

Figure 1: Range variation with Mach number for Boeing 747 (where l is the non-dimensional wing loading)

Further to considering this design problem, the design point is also considered here as a design variable, with Mach number and lift coefficient allowed to vary, however to fully model the trade-offs of speed, lift and drag with range, an induced drag penalty is also introduced. Hence the cost of a range-based optimization problem is close to equivalent to a single-point design problem and therefore much cheaper than a multi-point problem. The extra cost only comes from using one extra design variable in the optimization (Mach number). The overall goal is to consider an aerodynamic optimization problem which has an optimal solution that is shocked, allowing better overall performance across the design space.

The remainder of this paper is organised as follows: section II outlines the optimization framework used throughout this work; section III formally sets the range-based problem; analytical treatment of that problem is provided in section IV; sections V and VI give inviscid and viscous optimization results respectively; finally, conclusions are given in section VII.

[b]Mair and Birdsall plotted M against D/ML in Figure 10.15, however the inverse is plotted here

II. Optimization Framework

In this section, the overall optimization framework used for performing the aerodynamic optimizations outlined later is described. Both a global and gradient-based optimization approach are considered. This works alongside a reduced set of design parameters to minimize any chance of converging to a local minimum in the global case, and increase convergence speed in the gradient-based case. When used for the AIAA ADODG case 2[c], Iuliano [37] showed that the shape control scheme and gradient-based optimizer used in this work produced the largest drag reduction (also using the smallest number of design variables) of all results published for that case; the results are published in [16]. The geometry and mesh control scheme, optimizers and flow solver are described individually below. First, a formal definition of the optimization problem is given.

A generic single-objective optimization problem requires minimizing an objective function, J, which is a function of a vector of n design variables, $\boldsymbol{\alpha}$, subject to a set of inequality, $\mathbf{g}$, and equality, $\mathbf{h}$, constraints. Formally, this is written as:

$$\begin{aligned} \underset{\boldsymbol{\alpha}\in\Re^n}{\text{minimise}} \quad & J(\boldsymbol{\alpha}) \\ \text{subject to} \quad & \mathbf{g}(\boldsymbol{\alpha}) \leq \mathbf{0} \\ & \mathbf{h}(\boldsymbol{\alpha}) = \mathbf{0} \end{aligned} \tag{1}$$

II.A. Shape Control

The design variables used are from a singular value decomposition (SVD) approach [38], which decomposes a training library of aerofoils into constituent modes and this has the advantage of producing an optimal reduced set of shape modes according to the optimality theory of SVD[39].

To determine design variables using an SVD approach, a training library of aerofoils is collated. From this, shape variations between all of the aerofoils in the library are calculated to produce a variations matrix, $\mathbf{\Delta X}$. Performing an SVD then decomposes the variations matrix into a matrix of mode shapes, $\mathbf{U}$, a matrix of singular values, $\mathbf{\Sigma}$, and a weighting matrix, $\mathbf{V}$, where the decomposition is given by:

$$\mathbf{\Delta X} = \mathbf{U\Sigma V}^T \tag{2}$$

The mode shapes, which are the columns of $\mathbf{U}$, are then design parameters. Since the SVD process ranks mode shapes by their singular values, the $\mathbf{U}$ matrix can be truncated to the first n columns (where n is the required number of design variables in the optimization) to produce $\mathbf{U}'$. A new aerofoil shape, $\mathbf{X}^{new}$, is then

[c]This is lift-constrained, drag minimization of the RAE2822 in transonic, viscous flow.

given by a linear combination of n modes superimposed onto an initial aerofoil shape, $\mathbf{X}^{old}$:

$$\mathbf{X}^{new} = \mathbf{X}^{old} + \sum_{i=1}^{n} \alpha_i \mathbf{U}'_i \tag{3}$$

where $\mathbf{U}'_i$ is the i-th column of $\mathbf{U}'$ (i.e. the i-th mode). Hence the design variables in the optimization are the weightings of each modal deformation. The method has been shown to produce aerofoil design variables that are effective at inverse shape recovery [40] and aerofoil optimization [41], requiring as few as six design parameters to obtain optimum solutions in transonic drag minimization cases, however, shock-free solutions are more readily obtained with 12 design variables. As such, 12 modal design variables are used for the optimizations.

For suitable mesh deformation, an efficient domain element shape parameterization method has been developed by the authors and presented previously for CFD-based shape optimization [6, 42]. The parameterization technique, surface control and volume mesh deformation all use radial basis functions (RBFs), wherein global interpolation is used to provide direct control of the design surface and the CFD mesh, which is deformed in a high-quality fashion [43, 44]. A small set of control points are deformed using the modal design variables, which subsequently deforms the CFD mesh; figure 2 shows example exaggerated deformations of a mesh using two different modes.

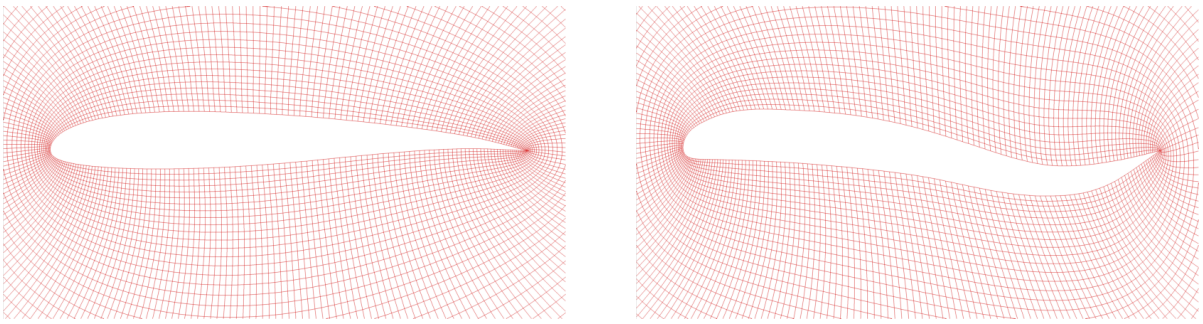

(a) Second mode

(b) Fourth mode

Figure 2: Exaggerated mesh deformation with two different modes

II.B. Optimizers

A global optimization approach is considered for inviscid optimizations (see section V) while a gradient-based approach is used for viscous optimizations (see section VI) due to the extra cost associated with the flow solve.

II.B.1. Global Optimizer

The global optimization algorithm used is an agent-based method, where a population of agents are used to traverse the design space in search of a solution. The location of an agent within the search space of n design variables is $\boldsymbol{\alpha} = [\alpha_1, \alpha_2, \ldots, \alpha_n]^T$, and in an agent-based optimization algorithm moves to a new location at the next iteration of the search by:

$$\boldsymbol{\alpha}(t+1) = \boldsymbol{\alpha}(t) + \mathbf{v}(t) \tag{4}$$

where $\mathbf{v}$ is the vector of location deformations, which is more commonly termed a particle's velocity, the determination of which separates various agent-based methods.

A hybrid of the particle swarm optimization (PSO) [45], and the gravitational search algorithm (GSA) [46] has been developed and used here such that the memory qualities of PSO complement the global transfer of data that occurs in GSA to obtain a highly efficient global search algorithm. Constraints are not directly handled in the PSO or GSA algorithms, hence the separation-sub-swarm (3S) [47] constraint handling method is applied. The 3S method is a constraint handling framework that can be applied to any swarm intelligence algorithm and works by splitting the overall population into two independent swarms every iteration – one swarm containing all of the feasible particles at that iteration (all constraints are satisfied) and one containing all of the infeasible particles at that iteration (at least one constraint is violated). The swarms then independently solve a different objective function, where the objective function of a particle ζ is determined by:

$$\zeta(\boldsymbol{\alpha}) = \begin{cases} J(\boldsymbol{\alpha}) & \text{if } \phi(\boldsymbol{\alpha}) = 0 \\ \phi(\boldsymbol{\alpha}) & \text{else} \end{cases} \tag{5}$$

where ϕ is the sum of the constraint violations. Hence, the infeasible particles have the objective of minimizing the constraint violation and therefore trying to find the feasible region whereas the feasible particles are minimizing the objective that is to be solved for.

The 3S algorithm has been shown to outperform other common constraint handling methods such as penalty methods [47]. The overall framework has also successfully been applied to inviscid and viscous aerofoil optimization [41] as well as wing optimization [48].

For all runs, a population size of 64 was used and run for 1500 iterations to ensure convergence. The population size was chosen based on previous studies using this optimizer by the authors [41], where between 50 and 100 individuals was sufficient for global optimization. The precise number was determine based on the architecture of the cluster used for the computations. Again, 1500 iterations was found to be more than

sufficient for this optimizer [41].

The optimizer uses a parallel decomposition of the search agent population where the objective evaluation for each agent is performed on its own processor, with updates being performed on the master processor. Hence the wall-time for each iteration is given by the cost of a single objective evaluation plus the optimizer update time.

II.B.2. Gradient-Based Optimizer

The gradient-based optimization algorithm is the feasible sequential quadratic programming (FSQP) algorithm as implemented in version 3.7 [49]. FSQP is based on the sequential quadratic programming (SQP) approach, but modified to improve convergence by combining a search along an arc [50] with a non-monotone procedure for that search [51]. The FSQP algorithm is fully described and analysed in [52, 53], though the basics of the implementation are described below.

Again, the vector of n design variables is given as $\boldsymbol{\alpha}$, which moves to the next location every major iteration along the arc given by:

$$\boldsymbol{\alpha}(t+1) = \boldsymbol{\alpha}(t) + a\Delta\boldsymbol{\alpha} + a^2\overline{\Delta\boldsymbol{\alpha}} \tag{6}$$

where a is the step size, $\Delta\boldsymbol{\alpha}$ is the step direction, which is found by a partition of unity-blend of the conventional SQP step direction and a feasible step direction, and $\overline{\Delta\boldsymbol{\alpha}}$ is a correction direction. The rules governing the construction of the step directions are given by Zhou *et al.* [49]. The conventional SQP step direction computation requires the Hessian and gradients. The Hessian is updated using the Broyden-Fletcher-Goldfarb-Shanno (BFGS) update scheme where the Hessian approximation is initialised as the identity matrix. The gradients are obtained by a second-order central-difference scheme, so the number of objective function evaluations is proportional to the number of design variables. The non-monotone line search then proceeds with the further modification being that a reduction in the objective function is required at $\boldsymbol{\alpha}(t+1)$ against the maximum objective from the previous four major iterations. This acts to further improve convergence [54]. The algorithm iterates until either the Kuhn-Tucker conditions are satisfied, or no step size can be found that maintains a feasible solution.

To further improve the efficiency of the computational implementation, the authors employ a parallel decomposition of the sensitivity evaluations based on the number of design variables. The sensitivity evaluation of the objective function and constraints with respect to the design variables is split between the number of CPUs available. Objective and constraint evaluations and optimizer updates occur on the master process, and each CPU controls the geometry (and CFD volume mesh) perturbations corresponding to the different design variables, and calls the flow solver. Flow solver results are then returned to the master for optimizer updates.

II.C. Flow Solver and Meshes

The flow solver used is a structured multiblock, finite-volume, cell-centred scheme solving the compressible Euler or Reynolds-Averaged Navier-Stokes (RANS) equations. The convective terms are evaluated using third-order upwind spatial approximation with the flux vector splitting of van Leer [55]. Diffusive terms are evaluated using second-order central differences, and turbulent viscosity is modelled by the Spalart-Allmaras one-equation model [56, 57]. Multi-stage Runge-Kutta with local timestepping is used for time integration, and convergence acceleration is achieved through V-cycle multigrid [58].

Since global optimization is performed, which requires large numbers of solver calls, careful selection of mesh density becomes very important. Meshes were created to minimise numerical drag as much as possible, though balancing the need to minimise run-time. For inviscid flows, a single-block O-mesh was generated using a conformal mapping approach. Figure 3 shows views of the 257×97 point mesh around the NACA0012, which extend to 100 chords at farfield. All surface cells have an aspect ratio of one.

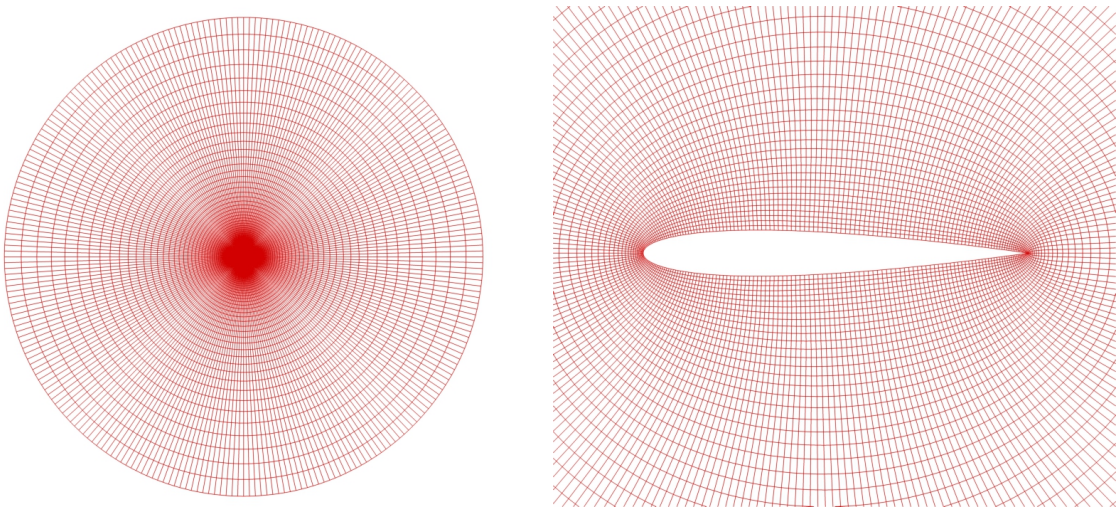

Figure 3: 257×97 NACA0012 O-meshes

For viscous flows, a three-block C-mesh was generated using the transfinite interpolation with improved orthogonality and smoothness method of Allen[59]. Figure 4 shows two views of the mesh which has 385 points around the aerofoil, 65 points along the wake line and 129 points into the farfield.

III. Consideration of Range Optimization with Varying Design Point

The majority of two-dimensional transonic aerodynamic optimizations seek to minimise drag at a fixed Mach number, with the consequence that aerofoil geometry is modified to force solutions that are shock-free. As noted in the introduction, shock-free design is well known to degrade off-design behaviour at different Mach number points, as by Morawetz's proof [20] and Drela's demonstrations [32]; a shock-free solution is

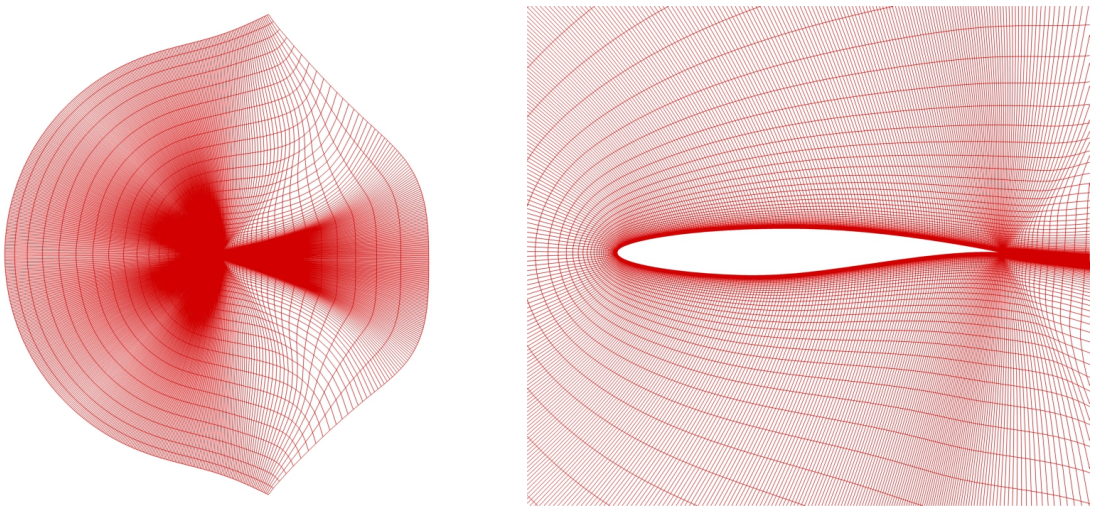

Figure 4: Three-block RAE2822 viscous C-mesh

strongly local. In addition, aircraft design is not driven purely by drag, and an objective that typifies the industrial process more closely is optimizing the range, r, which for a cruising, jet-powered aircraft is given by the Brequet range equation:

$$r = \frac{u}{c}\frac{L}{D}\log\left(\frac{W_1}{W_2}\right) \tag{7}$$

where u is the aircraft velocity, c is the specific fuel consumption (SFC), L and D are the lift and drag, and W_1 and W_2 are the initial and final cruise weights respectively. Under the assumption of constant speed of sound through cruise (so $u \propto M$) and constant SFC, the range factor can be extracted, $R = ML/D$, which can be used as the objective function in optimization. The equivalent expression using non-dimensional force coefficients is $R = MC_L/C_D$. In this scenario, the aerodynamic optimization problem is enriched with the operating point (characterized by M and C_L), which is allowed to vary. A similar optimization problem has also be considered by Buckley and Zingg [30], albeit for low-speed UAV design. The work here expands into inviscid and viscous transonic aerofoil design, and puts this type of optimization problem in the context of suitability for design.

It is also worth noting that a simplified engine model can also be introduced to change the assumption of constant SFC. For example, Jameson *et al.* [60] assumed that $c \propto \sqrt{M}$, hence this leads to a range factor of $\sqrt{M}L/D$. Using this simplified model would likely alter the optimum design point. However, in this work the MC_L/C_D factor is considered since it is the trade-offs in the aerodynamic performance that are studied.

Before attempting geometric optimization it is useful to consider the optimization of the operating point in isolation. A common optimization approach is to constrain C_L, however, this is not suitable in a process where Mach number varies, as equilibrium flight at a fixed weight demands a fixed dimensional lift. A

more appropriate constraint is therefore $M^2 C_L$, which is a non-dimensional measure of wing loading ($\frac{W}{S} = C_L \frac{1}{2}\gamma M^2 P$). This means that there is only a single free parameter, Mach number, with the aerofoil trimmed to achieve the required lift coefficient for that Mach number. The optimization problem is therefore written as:

$$\begin{aligned} \underset{M}{\text{maximise}} \quad & M\frac{C_L}{C_D} \\ \text{subject to} \quad & M^2 C_L = l \end{aligned} \tag{8}$$

where the parameter, l, is some non-dimensional wing loading that must be maintained to yield the same physical lift. In the purely unconstrained problem, where range is maximised with no lift constraint, assuming two-dimensional inviscid flow, the solution is known to be the critical Mach number (the Mach number at which flow over the body first becomes sonic). However, by realistic selection of the lift constraint, a transonic, and shocked solution can be forced.

While it is useful to consider the isolated effect of changing Mach number, the usual aerodynamic optimization process involves modifying some shape to improve the objective. Often this is subject to an internal volume (V) requirement to represent the need to house structure or fuel. Hence, if any general shape changes are included, defined here by a vector, $\mathbf{\Delta x}$, the full optimization problem is now described as:

$$\begin{aligned} \underset{\mathbf{\Delta x}, M}{\text{maximise}} \quad & M\frac{C_L}{C_D} \\ \text{subject to} \quad & M^2 C_L = l \\ & V \geq V_{initial} \end{aligned} \tag{9}$$

In the context of optimization, the cost of solving problem 9 is similar to that of a single-point drag minimization. The cost associated with adding a further design variable in both optimizers is small. Hence, the multi-point optimization is performed using N design points, so the single-point and range-based optimizations offers a cost reduction of $O(N)$ of the cost of the multi-point. However, while the cost is lower for range-based optimization, it is worth noting that the primary disadvantage of considering this is the context of aircraft optimization is that improvement at a specified design condition is not the goal (as it would be in point optimization). For the work considered in this paper this is not a problem since the objective here is to consider the effect of a range-based problem on the resulting optimal geometries.

An interesting aspect of this problem is that in the circumstance of fixing the design point, the problem reduces to that of a single-point drag minimization. Hence, it would be theoretically possible, though prohibitively expensive, to obtain similar results if the M-C_L space was densely sampled and a single-point drag minimization performed at each of those sample points.

IV. Analytical Treatment for Fixed Shape

Before performing geometric optimization, which is presented later, an analytical treatment is considered, first, for optimizing the problem described by problem 8, to find a value of M that maximizes the Breguet range parameter. This involves differentiating the Breguet range parameter with respect to the design variable, which is Mach number. This is performed by considering inviscid flow, so the only source of drag is due to the shock. An analytical approximation of wave drag is used to approximate the optimal solution.

IV.A. Expression for Optimal Mach

A useful (but approximate) analytical result for wave drag is 'Lock's fourth power result'[61], which may be used to gain insight in to this problem. It should be noted that Lock's result as used here is suitable for showing trends and relative comparisons, but it is not an accurate method for finding absolute values of wave drag on aerofoils owing to the restrictive assumptions used in the derivation. Lock's approximation is based on a calculation of wave drag that uses an integration of the normal shock relations along the face of the shock. This principle itself is exact, but does not lead to a straightforward algebraic form. For that reason, Lock further assumed a particular variation of upstream Mach number along the shock face, and also assumed a particular variation of shock height with freestream Mach number. Lock also assumed that the shock forms, and remains, at the incompressible $C_{p_{min}}$ location. It is these assumptions that limit the accuracy of the method, but which at the same time also permit a very practical analytical result where none would otherwise be possible.

The final results of this analysis are that drag per unit height of a normal shock scales with the third power of the Mach number above the critical Mach number, M_c, ie. $M - M_c$, while the shock height is also proportional to $M - M_c$, finally giving a drag proportional to a fourth power. A calibration constant k also appears in front of the final result to give an expression for wave drag, C_{D_w}, as:

$$C_{D_w} = k(M - M_c)^4 \tag{10}$$

Although k can be found through treatment of incompressible data, it is more straightforward and accurate to use two-dimensional transonic CFD. Lock's work was originally aimed at deriving a measure of compressible aerofoil performance superior to only considering critical Mach number, for which Lock proposed the use of k, but the Mach-drag scaling remains useful in the transonic regime, where analytical results, however approximate, are relatively rare. The objective here is to apply this in the context of a constrained ML/D operating point. Since Lock's result uses M_c as a reference Mach number, the influence of lift on wave drag is included in addition to the effect of Mach number, because any increase in lift corresponds to a lower

value of M_c, thus raising drag (the critical Mach number drops as the minimum C_p becomes more negative, which is equivalent to higher C_l at incompressible speeds).

The physical trade-off for the operating point is very important. At low Mach, lift coefficient must be high. This drives a low critical Mach number and consequently a higher wave drag. At high Mach, the wave drag naturally increases due to the increased offset from M_c. It follows that in between these extremes there lies an optimum where neither the lift coefficient nor Mach number are too high, and it is this optimum that shall be explored with a basic analytical treatment. It is shown that transonic results arise naturally if M^2C_L is large for the problem given by problem 8 (where the only design variable is Mach number).

The Breguet range parameter is:

$$R = \frac{MC_L}{C_D} \tag{11}$$

Multiplying by M gives a numerator that that will have zero gradient with respect to Mach number when the lift constraint is satisfied.

$$R = \frac{M^2C_L}{MC_D} \tag{12}$$

The only important factor in this analysis is the wave drag, C_{D_w}, however, C_D is given by the sum of the wave drag and the drag due to other effects, which in this analysis are termed C_{D_0}. Wave drag is given by equation 10, hence equation 12 becomes:

$$R = \frac{M^2C_L}{MC_{D_0} + Mk(M - M_c)^4} \tag{13}$$

At the optimum solution, the gradient of the objective with respect to the design variable is zero. To find the optimal Mach, equation 13 (the objective function) is therefore differentiated with respect to M (the design variable) to give:

$$\frac{dR}{dM} = \frac{MC_D\left(\frac{d(M^2C_L)}{dM}\right) - M^2C_L\left(C_{D_0} + k(M - M_c)^4 + 4Mk(M - M_c)^3\left(1 - \frac{dM_c}{dM}\right)\right)}{M^2C_D^2}$$

It should be noted that for simplification, some of the C_D terms are kept as $C_D = C_{D_0} + C_{D_w}$. The result is set to zero (noting that M^2C_L is constant so its gradient is zero):

$$F = C_{D_0} + k(M - M_c)^4 + 4Mk(M - M_c)^3\left(1 - \frac{dM_c}{dM}\right) = 0 \tag{14}$$

Equation 14 is the resulting polynomial that dictates the optimal condition for the range parameter, and solving allows the optimal Mach number that maximises range to be found. This involves finding M_c and

dM_c/dM. The critical Mach number must be differentiated, which is achieved by writing the derivative as:

$$\frac{dM_c}{dM} = \frac{dM_c}{dC_{p_{min}}} \frac{dC_{p_{min}}}{dC_{L_{incomp}}} \frac{dC_{L_{incomp}}}{dM} \tag{15}$$

where $C_{p_{min}}$ is the minimum pressure coefficient on the aerofoil surface and $C_{L_{incomp}}$ is the incompressible lift coefficient of the aerofoil. In this expression the first term is positive, because M_c falls as $C_{p_{min}}$ becomes more negative, the second term is negative because $C_{p_{min}}$ falls as $C_{L_{incomp}}$ rises and the third term is negative because $C_{L_{incomp}}$ drops as M goes up (higher Mach number corresponds to lower lift at same angle at incompressible speed). This implies that the overall derivative is positive, and the value varies from zero (at low speeds M_c is independent of M) to over unity (at high speed, as M rises the equivalent incompressible C_L drops, so that M_c can rise faster than M). Calculation shows that it is typically between 1.0 and 1.1 at transonic Mach numbers.

The next steps will seek to calculate the three terms on the right hand side of equation 15 moving right to left. The first term considered is $dC_{L_{incomp}}/dM$, so a result is needed to link the compressible lift coefficient to the incompressible one at the same angle of attack i.e.

$$C_L = \frac{l}{M^2} = f(M) C_{L_{incomp}} \tag{16}$$

Below critical speeds a Prandtl-Glauert or similar correction is suitable, but at supercritical conditions an empirical adjustment is needed, a suitable type being:

$$f(M) = \frac{1}{\sqrt{1-M^2}} \left(1 + k_1 M^{p_1}\right) \left(1 - \left(\frac{M}{M_0}\right)^{p_2}\right) \tag{17}$$

Equation 17 represents the conventional Prandtl-Glauert correction modified such that deviations at higher Mach numbers are better captured. Typical constants are $k_1 = 9$, $p_1 = 10$, $M_0 = 0.935$ and $p_2 = 8$ for NACA0012, or $k_1 = 12.5$, $p_1 = 10$, $M_0 = 0.888$ and $p_2 = 8$ for RAE2822, obtained by performing a least squares fit to computational data; these constants must generally be estimated for a new aerofoil by CFD or experimental means. For the remainder of this analysis the (M) notation is dropped for the $f(M)$ expression, hence $f \equiv f(M)$.

The lift constraint is given by $M^2 C_L = l$. Substituting in equation 16, and the incompressible lift coefficient can be written as:

$$C_{L_{incomp}} = \frac{l}{M^2 f} \tag{18}$$

Hence, the third term in equation 15 can now be evaluated by differentiating equation 18 (as before, l is a

constant so that $\frac{dl}{dM} = 0$), which gives:

$$\frac{dC_{L_{incomp}}}{dM} = \frac{M^2 f \frac{dl}{M} - l(2Mf + M^2 \frac{df}{dM})}{M^4 f^2} = \frac{-l(2Mf + M^2 \frac{df}{dM})}{M^4 f^2} \tag{19}$$

Now consider the second term on the right hand side of equation 15 ($dC_{p_{min}}/dC_{L_{incomp}}$). To evaluate this term, the minimum surface pressure coefficient must be parameterized by the incompressible lift coefficient. The following $C_{p_{min}}$ relation is observed to be reasonable (although deviations from linearity exist on a small scale):

$$C_{p_{min}} = a + bC^2_{L_{incomp}}$$

Performing the differentiation to give $dC_{p_{min}}/dC_{L_{incomp}}$:

$$\frac{dC_{p_{min}}}{dC_{L_{incomp}}} = 2bC_{L_{incomp}} \tag{20}$$

Constants are typically determined through a panel calculation and least-squares fit ($a = -0.529$, $b = -4.079$ for NACA 0012 and $a = -0.132$, $b = -4.596$ for RAE 2822).

The final step is to evaluate the first term on the right hand side of equation 15 ($dM_c/dC_{p_{min}}$). This involves finding an expression for dC^*_p/dM_c (where C^*_p is the critical pressure coefficient) and also specifying some function, g, of the 1) minimum surface pressure coefficient on the aerofoil and 2) critical Mach number i.e. $C^*_p(M_c) = g(C_{p_{min}}, M_c)$. A suitable form for the function is the Prandtl-Glauert correction:

$$g = \frac{C_{p_{min}}}{\sqrt{1 - M_c^2}}$$

Differentiating this with respect to $C_{p_{min}}$:

$$\frac{dC^*_p}{dM_c}\frac{dM_c}{dC_{p_{min}}} = \frac{\partial g}{\partial M_c}\frac{dM_c}{dC_{p_{min}}} + \frac{\partial g}{\partial C_{p_{min}}}$$

Rearranging:

$$\frac{dM_c}{dC_{p_{min}}} = \frac{\frac{\partial g}{\partial C_{p_{min}}}}{\frac{dC^*_p}{dM_c} - \frac{\partial g}{\partial M_c}} \tag{21}$$

To evaluate equation 21, the isentropic flow relation needs to be differentiated. The critical pressure coefficient (as a function of freestream Mach number) is:

$$C^*_p = \frac{2}{\gamma M^2_\infty}\left(\frac{p}{p_0}\frac{p_0}{p_\infty} - 1\right) = \frac{2}{\gamma M^2_\infty}\left(\frac{1}{1.895}\left(1 + \frac{\gamma - 1}{2}M^2_\infty\right)^{\frac{\gamma}{\gamma-1}} - 1\right) \tag{22}$$

Differentiating this with respect to the freestream Mach number leads to (dropping the ∞ notation so $M \equiv M_\infty$):

$$\frac{dC_p^*}{dM} = \frac{2}{1.895\gamma M^2}\left(M\gamma\left(1+\frac{\gamma-1}{2}M^2\right)^{\frac{1}{\gamma-1}}\right) - \frac{4}{\gamma M^3}\left(\frac{1}{1.895}\left(1+\frac{\gamma-1}{2}M^2\right)^{\frac{\gamma}{\gamma-1}} - 1\right) \tag{23}$$

Finally, the function g must also be differentiated. For the Prandtl-Glauert correction this becomes:

$$\frac{\partial g}{\partial M} = \frac{C_{p_{min}} M}{(1-M^2)^{\frac{3}{2}}} \tag{24}$$

$$\frac{\partial g}{\partial C_{p_{min}}} = \frac{1}{\sqrt{1-M^2}} \tag{25}$$

To find the first term of equation 15, equations 23, 24 and 25 are evaluated and substituted into equation 21.

All three terms in equation 15 have now been evaluated. Returning now to equation 14, it is assumed that the flow is inviscid and in two dimensions so C_{D_0} can be ignored, and it is also assumed the flow is transonic, so $M > M_c$ (otherwise C_{D_w} is undefined) meaning there is a positive amount of drag, which is wave drag only, and gives the optimum Mach number, M_{opt}, for maximizing range subject to a constraint on fixed loading as:

$$M_{opt} = \frac{M_c}{5 - 4\frac{dM_c}{dM}} \tag{26}$$

To solve this, an outer bisection loop on M_{opt} is used, with M_c found through an inner bisection loop. dM_c/dM is calculated thereafter from equation 15 using the calculated M_c.

IV.B. Results

First, it is interesting to explore the shape of the governing polynomial (equation 14), with the caveat that two-dimensional inviscid flow is considered (meaning $C_{D_0} = 0$) and any roots to the left of M_c are non-physical. Figure 5 shows the polynomial for NACA 0012 alongside the M_c values; it is important to note that the M_c value plotted corresponds to the M_c value for the rightmost root, therefore, the M_c does not necessarily correspond to a root of the plotted function (this is intrinsic because M_c is a function of M due to the $M^2 C_L$ constraint). Indeed, this is the important point to note from the function shape, because for $l > 0.15$ the root is to the right of M_c, i.e. it is transonic. The limit case is also shown, illustrating that, as expected, in this scenario for $l = 0.15$, the optimum Mach number sits just on top of the root of the function, and for any higher value of l the root shifts to the right of M_c and becomes transonic. For any lower value

there will be no root to the right of M_c.

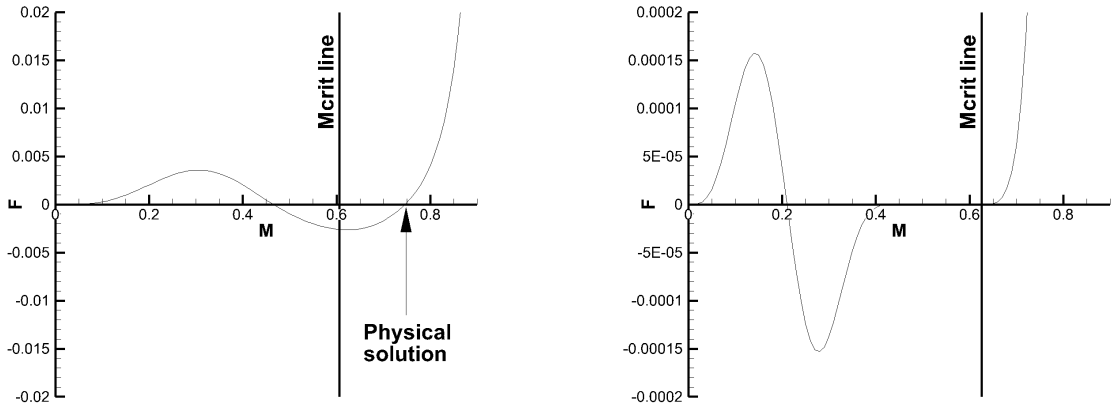

(a) $l = 0.35$ (b) limit case $l = 0.15$

Figure 5: Comparison of constraint influence on M_{opt} for NACA 0012

Table 1 shows the M_{opt}/M_c values for varying l for the NACA0012, indicating that the value of 1.23 for $l = 0.35$ compares reasonably to the CFD value of 1.33 (see below), at least to a margin consistent with the assumptions underpinning Lock's relationship. Further increases in l drive a trend towards a higher M_c, consistent with the root in figure 5 being driven to the right as the function curves increasingly below the axis. Lock's result is limited in accuracy, but it gives a clear indicator of a transonic optimal point in this case (i.e. where $M_{opt}/M_c \geq 1$).

Table 1: Analytical optimal Breguet Mach numbers as a fraction of M_c for NACA 0012 using M^2C_L as a constraint

l	M_{opt}/M_c
0.20	1.071
0.25	1.149
0.35	1.23
0.45	1.288
0.55	1.34
0.60	1.366

A final interesting point is what value of l necessitates a transonic optimum. This is found from enforcing $M_{opt} = M_c$, which may be done with a bisection loop around the analytical root solver. This reveals that for the NACA 0012 case $l = 0.15$ is the approximate limiting value, while the equivalent value for RAE 2822 is $l = 0.26$. Below these watershed points it is possible to find a subcritical optimal point that satisfies the constraint, whilst above this only a supercritical optimal condition is possible.

IV.C. Numerical Correlation

The primary reason for considering this case is to produce an optimal solution that has a shock such that point design is avoided. If the M^2C_L constraint is sufficiently large, at low M it is seen that C_L must rise to compensate, lowering M_c and increasing wave drag, whilst at high M, increases in M eventually outpace any increase in M_c and wave drag again rises. In between these extremes must lie an optimum, and whether or not it is transonic depends on the value of l that is used. Figure 6 shows sweeps in M computed with inviscid CFD for NACA 0012 and RAE 2822 (each point was trimmed to the appropriate C_L value for that M), illustrating that for NACA 0012 at $l = 0.35$, $M_{opt} = 0.65$ to within the sweep resolution (and since $M_c = 0.49$ for this trim point, $\frac{M}{M_c} = 1.33$, compared to an analytical prediction of 1.23), while for 2822 at $l = 0.45$, $M_{opt} = 0.7$ (and $M_c = 0.55$ so for this trim point, $\frac{M}{M_c} = 1.27$).

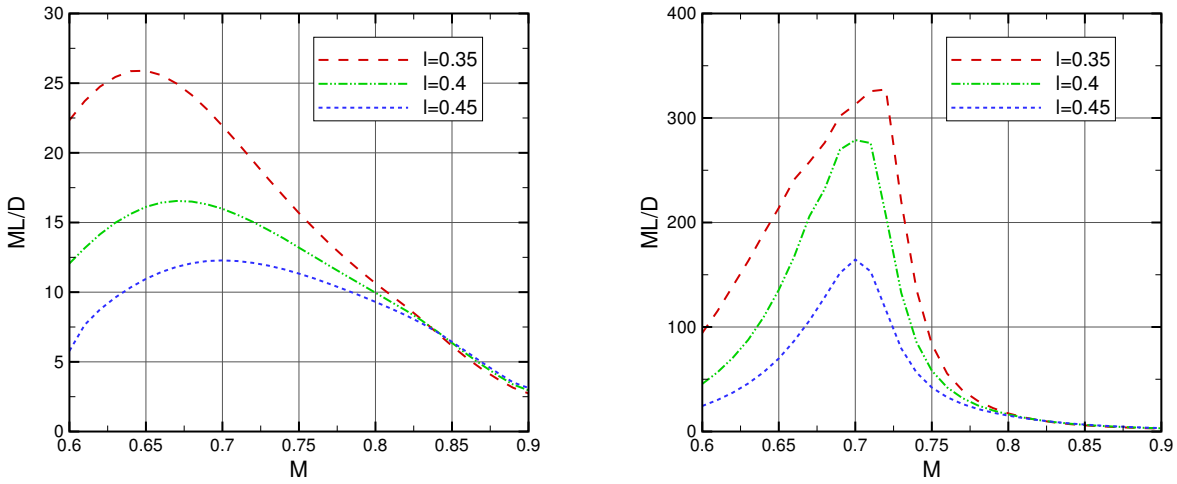

(a) NACA 0012

(b) RAE 2822

Figure 6: Mach sweeps at fixed l showing ML/D

The limited accuracy of the Lock result means that the absolute value of the optimal Mach number differs between the algebraic and the CFD (0.75 versus 0.65 for NACA0012, and 0.8 versus 0.7 for RAE2822) by some margin, but as a fraction of M_c the agreement is surprising. Also, Lock notes [61] an offset in drag rise as a function of Mach of 0.1, which is observable compared to CFD and attributable to the compressible flow simplifications in his analysis, and a similar shift subtracting an increment of 0.1 in optimal Mach number would bring the absolute results much closer to CFD.

V. Inviscid Range Optimizations

In this section, a brief investigation is presented on performing range optimizations in inviscid flow. The optimizations presented here are used as numerical validation of the simple concepts introduced in the

analytical treatment, and act as a proof-of-concept for solving problem 9 in preparation for a more substantial study of optimization in viscous flow (presented later). All optimizations were performed using the global optimizer (see section II.B.1) due to the lower cost associated with performing the objective evaluations (compared to the viscous results).

Before progressing, care has to be taken in the construction of the optimization problem. Now that Mach number is a design variable, its influence on the aerodynamic design problem needs to be fully captured. This is only strictly possible in full three-dimensional wing optimization, where induced drag is captured. Hence, for the aerofoil optimizations, an induced drag coefficient $C_{D_i} = \kappa C_L^2$ (where κ is the induced drag coefficient and $\kappa = 1/\pi AR$) is added to model these trade-offs and to penalise the negative effect of higher lift coefficients that would exist in three-dimensional wing design. The range parameter including this induced drag term, R_κ, is introduced:

$$R_\kappa = M \frac{C_L}{C_D + \kappa C_L^2} \tag{27}$$

The optimization problem now being considered is given by:

$$\begin{aligned} \underset{\boldsymbol{\alpha}, M}{\text{maximise}} \quad & M \frac{C_L}{C_D + \kappa C_L^2} \\ \text{subject to} \quad & M^2 C_L = l \\ & V \geq V_{initial} \end{aligned} \tag{28}$$

While the effect of adding this factor is to mimic the trade-offs that occur between speed, lift, drag and range, it is interesting to note how this occurs. This factor adds a penalty due to lift to the denominator of the objective function. Hence, a change in the Mach number, which may lead to the shock forming leads to a change in C_L due to the lift constraint. As long as the change in the lift coefficient is greater than the change in the drag coefficient due to the shock, then the shock is permitted. Due to C_L appearing on the numerator and denominator of the objective function, this change will at some point balance out to result in a shocked optimum.

Range optimizations are now presented for the NACA0012 at three different values of non-dimensional wing loading: $l = 0.35, 0.4, 0.45$. An initial set of optimizations are presented for no induced drag penalty ($\kappa = 0$) to provide a datum. For these optimizations, the shape and Mach number are allowed to change with a constraint placed on the internal volume. The optimization results are presented in table 2 and the surface pressure coefficients and surface Mach numbers of the optimized results are shown in figure 7.

The three optimizations have produced shock-free solutions. Furthermore, as was shown in the analytical treatment, higher values of l result in lower optimum range factors, which was also found in the optimization

Table 2: Results for inviscid range optimizations

l		C_L	C_D	M	R
0.35	Initial	0.56	0.0425	0.800	10.5
	Optimized	0.73	0.0017	0.702	301.4
0.40	Initial	0.63	0.0513	0.800	9.8
	Optimized	0.88	0.0023	0.680	260.2
0.45	Initial	0.71	0.0607	0.800	9.4
	Optimized	0.92	0.0025	0.701	258.0

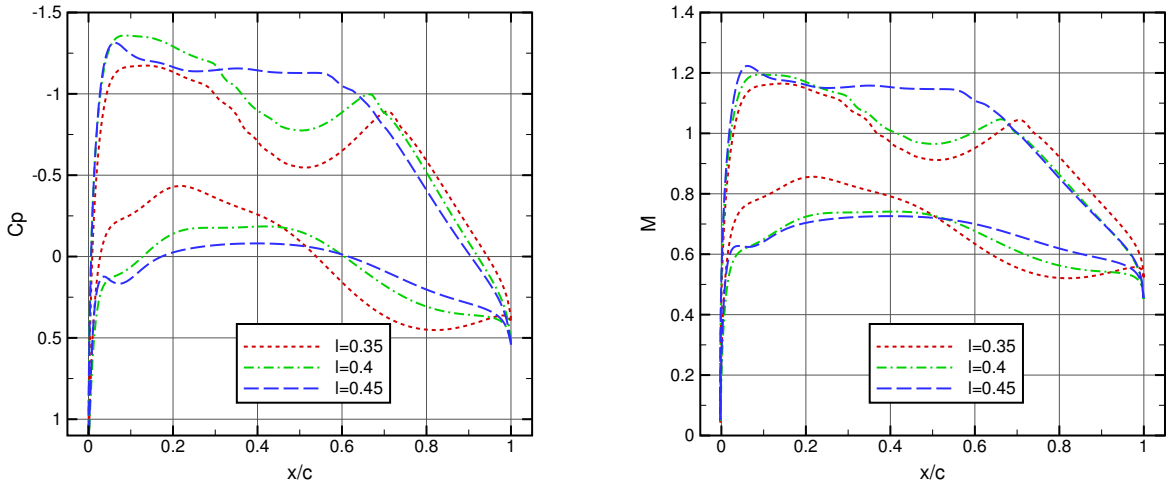

(a) C_P (b) Mach

Figure 7: Surface C_P and Mach number for inviscid range optimizations

results. However, in the analytical treatment it was also shown that the optimum is supercritical assuming that the lift value chosen is sufficiently high, but this does not necessarily lead to a shocked solution and, in fact, all of the optimizations presented in figure 7 are supercritical (as shown in the surface Mach plot in figure 7), though shock-free. If freestream Mach number was to be increased further, to where a shock forms, then wave drag increases approximately with the fourth power of Mach number, according to Lock[61]. The subsequent increase in objective function due to the increase in Mach number is offset by the reduction in objective function due to the increase in wave drag. Hence, the optimizer has increased lift coefficient to maximise the objective function, at the expense of higher Mach numbers leading to a shock-free solution.

Optimizations for a value of induced drag representative of a wing with aspect ratio 7.95–which is reasonably typical for a conventional jet-powered airliner–($\kappa = 0.04$) are now presented. Table 3 shows the results for these while figure 8 shows the optimized pressure distributions for these optimizations. The induced drag penalty has acted to lower the optimal lift coefficient and to increase the optimal Mach against

not having an representation of induced drag. It is clear that for an induced drag penalty factor that is a representative value, shocked optima result for all four of the l values considered. The general trend in the optimum solution with an increasing value of l is that the optimum Mach number reduces. The reduction in the optimal range that would result from a lower Mach number is compensated for by a greater increase in lift coefficient, indicating that any further increase in the Mach number would substantially increase the wave drag.

Table 3: Results for inviscid range optimizations with $\kappa = 0.04$ induced drag factor

l		C_L	C_D	C_{D_i}	M	R_κ
0.30	Initial	0.47	0.0342	0.0088	0.800	8.7
	Optimized	0.48	0.0011	0.0091	0.789	37.1
0.35	Initial	0.56	0.0425	0.0125	0.800	8.1
	Optimized	0.58	0.0015	0.0133	0.787	30.8
0.40	Initial	0.63	0.0513	0.0159	0.800	7.5
	Optimized	0.67	0.0020	0.0175	0.781	26.8
0.45	Initial	0.71	0.0607	0.0202	0.800	7.0
	Optimized	0.76	0.0023	0.0232	0.768	23.8

The final surface shapes of each of these optimizations are shown in figure 8 demonstrating that not only are shocked solutions forced, but that the global form of the surfaces are reasonably independent of the value of l chosen for a fixed κ. It is also interesting to note that the resulting shapes are supercritical in nature, displaying the flat upper surface pressure distribution with delayed shock, and the trailing edge cusp. This result is particularly promising considering the aerofoils were all initialised as a NACA0012.

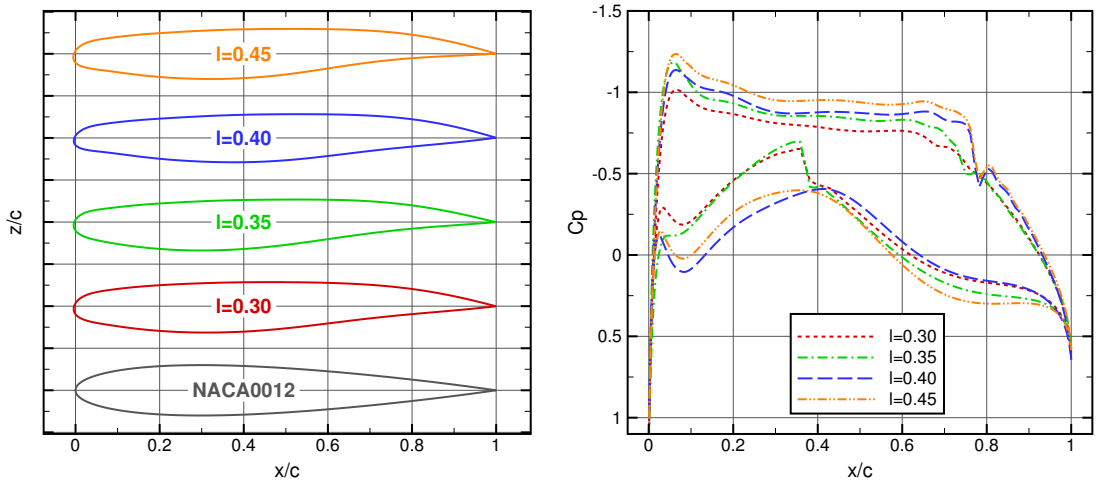

Figure 8: Surface shapes and C_P for inviscid range optimizations of NACA0012 at different lift values with induced drag penalty

VI. Comparison of Approaches for Viscous Optimization

While inviscid optimizations demonstrate that a range problem produces optimal solutions with shocks, it is also important to consider transonic viscous optimizations. Furthermore, it is also necessary to consider the differences that result from single- and multi-point optimizations. Hence, in this section, single- and multi-point, and range optimizations for a transonic viscous flow around an RAE2822 aerofoil are considered.

All viscous runs were performed using the FSQP gradient-based optimizer (see section II.B.2). While performing a small number of viscous global optimizations is possible, it has been shown by Chernukhin and Zingg [62] that gradient-based optimization is sufficient for viscous aerofoil optimization due to the design space being unimodal.

VI.A. Single-Point and Multi-Point Optimization

A single-point drag minimization is presented on the RAE2822 at a fixed design point to create a baseline result against which to compare. The problem is given by:

$$\begin{aligned} \underset{\boldsymbol{\alpha}}{\text{minimise}} \quad & C_D \\ \text{subject to} \quad & C_L \geq C_{L_{initial}} \\ & V \geq V_{initial} \end{aligned} \tag{29}$$

Second, a multi-point optimization is also presented. The conventional weighted-sum approach, where the overall objective function is a weighted sum of the objective from the individual design points, is considered. A lift constraint on each of the design points is used as well as the volume constraint on the overall shape. For N design points, where each has an objective weighting, $\lambda^{(i)}$, the multi-point optimization problem is therefore given as:

$$\begin{aligned} \underset{\boldsymbol{\alpha}}{\text{minimise}} \quad & \sum_{i=1}^{N} \lambda^{(i)} C_D^{(i)} \\ \text{subject to} \quad & C_L^{(i)} \geq C_{L_{initial}}^{(i)} \qquad (1 \leq i \leq N) \\ & V \geq V_{initial} \end{aligned} \tag{30}$$

The two design points for the cases are based on those studied by Drela [32], and are chosen such that they are suitably different within the operating space of the aerofoil. They are (the value for l is also calculated and given for comparison later):

Condition 1: $M = 0.68$, $C_L = 0.73$, $(l = 0.34)$ $Re = 6.5 \times 10^6$

Condition 2: $M = 0.74$, $C_L = 0.73$, $(l = 0.40)$ $Re = 6.5 \times 10^6$

where the single-point optimization is performed on case 2 and the multi-point optimization is performed for equal weightings on each case, hence the objective is $\frac{1}{2}C_D^{(1)} + \frac{1}{2}C_D^{(2)}$. As before, 12 modal design parameters are used for the surface deformations.

The results of the viscous optimizations are given in table 4. The final drag value of the single-point case at design condition 2 (which is the optimized condition) is slightly lower than the drag value of the multi-point case at the same condition and this is to be expected since the trade-off with the second design condition in the multi-point case restricts, somewhat, the result compared to considering one design point in isolation.

Table 4: Results for drag minimizations

	Condition 1			Condition 2			
	C_L	C_D	ΔC_D (%)	C_L	C_D	ΔC_D (%)	V
Initial	0.73	0.0150	-	0.73	0.0202	-	0.078
Single-point	-	-	-	0.73	0.0146	**-27.7%**	0.078
Multi-point	0.73	0.0145	**-3.3%**	0.73	0.0147	**-27.2%**	0.078

The surface shapes of the two optimizations (given in figure 10) as well as the resulting pressure coefficients (given in figure 9) differ considerably. Both solutions reduce the lift over the forebody of the aerofoil to minimise the leading edge acceleration and therefore avoid a shock forming while the lift is recovered closer to the trailing edge. However, the suction peak for condition 2 is pronounced in the single-point case, whereas this is more suppressed in the multi-point. The multi-point case has resulted in a slightly more cambered aerofoil. Clearly, the addition of condition 1 to the optimization has meant a slight compromise has been required in the multi-point optimization, which is unsurprising.

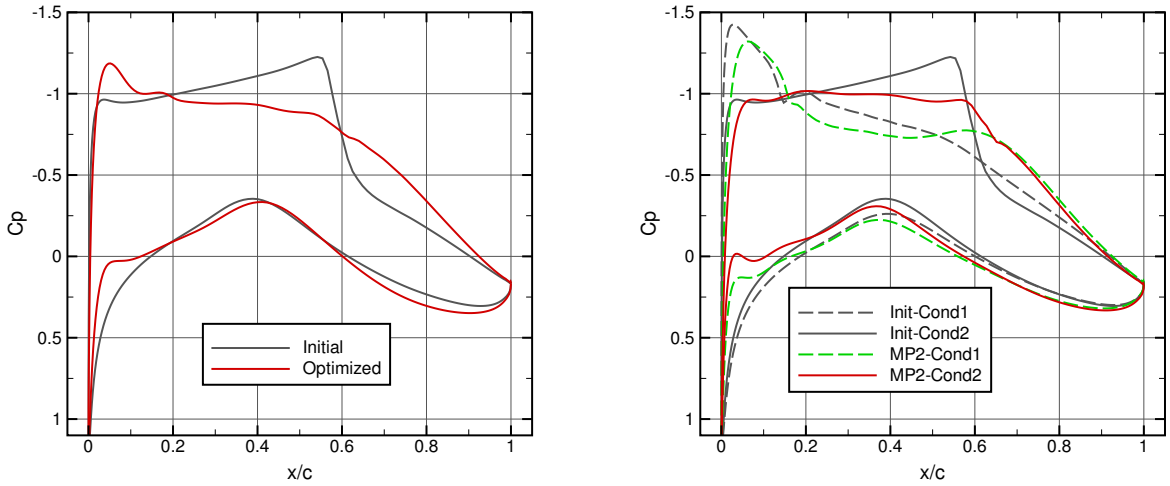

(a) Single-point (b) Multi-point

Figure 9: Surface C_P for single- and multi-point drag minimizations

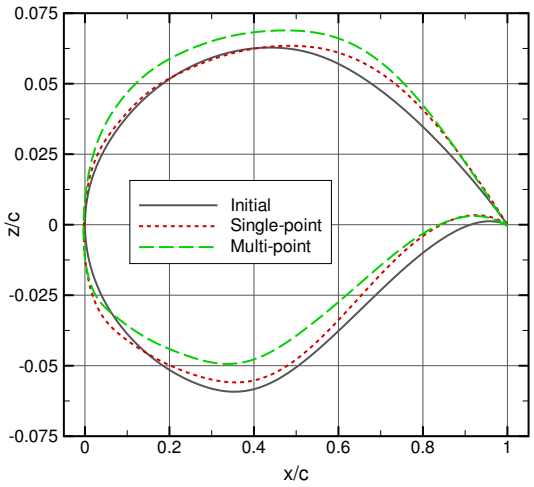

Figure 10: Surface shapes for drag minimizations

VI.B. Range Optimization

Range optimizations for viscous flow are now considered. As demonstrated in the inviscid optimizations, a lift-based penalty has to be added to the denominator of the range factor in the form of an induced drag expression to model the penalty that high lift coefficients have. As such, the viscous range optimization is also performed with the induced drag factor considered in the inviscid cases, though two values are considered here: $\kappa = 0.04$ and $\kappa = 0.1$. The starting aerofoil is the RAE2822, which is in flow at $Re = 6.5 \times 10^6$ (as per the drag minimizations).

The final optimization results are given in tables 5 and 6. The first clear trend is that for increasing non-dimensional wing loading, the optimum range reduces for both induced drag penalties considered.

Furthermore, the increase in induced drag penalty means that higher lift coefficients are penalised so the resulting optimum design point is at a higher Mach number and lower lift coefficient. These were both seen in the inviscid results, so these trends are expected.

Table 5: Results for viscous range optimizations with $\kappa = 0.04$

l		C_L	C_D	C_{D_i}	M	R_κ
0.30	Initial	0.53	0.0259	0.0112	0.750	11.2
	Optimized	0.49	0.0128	0.0097	0.780	17.0
0.35	Initial	0.63	0.0336	0.0159	0.750	9.5
	Optimized	0.60	0.0136	0.0141	0.770	16.6
0.40	Initial	0.71	0.0430	0.0202	0.750	8.4
	Optimized	0.67	0.0146	0.0178	0.774	16.0
0.45	Initial	0.80	0.0558	0.0256	0.750	7.4
	Optimized	0.82	0.0159	0.0265	0.743	14.3

Table 6: Results for viscous range optimizations with $\kappa = 0.1$

l		C_L	C_D	C_{D_i}	M	R_κ
0.30	Initial	0.53	0.0259	0.0281	0.750	7.4
	Optimized	0.47	0.0138	0.0219	0.801	10.5
0.35	Initial	0.63	0.0336	0.0397	0.750	6.4
	Optimized	0.55	0.0154	0.0308	0.798	9.6
0.40	Initial	0.71	0.0430	0.0504	0.750	5.7
	Optimized	0.68	0.0163	0.0467	0.766	8.3
0.45	Initial	0.80	0.0558	0.0640	0.750	5.0
	Optimized	0.74	0.0207	0.0547	0.780	7.7

The surface pressure distributions of the range optimizations are given in figure 11 and the surface shapes in figure 12. An interesting result is that despite the fact that an induced drag penalty has been added, the $\kappa = 0.04$ value is not enough to force a shocked solution. This is further shown in figure 13, which gives the field pressure contours of the optimizations at the two different induced drag values at $l = 0.35$, which clearly show that the lower value is not sufficient to penalise a shock-free solution. On the other hand, moving to a higher induced drag factor is enough to create an optimum at a high enough Mach and C_L combination such that a shock-free optimum is not possible.

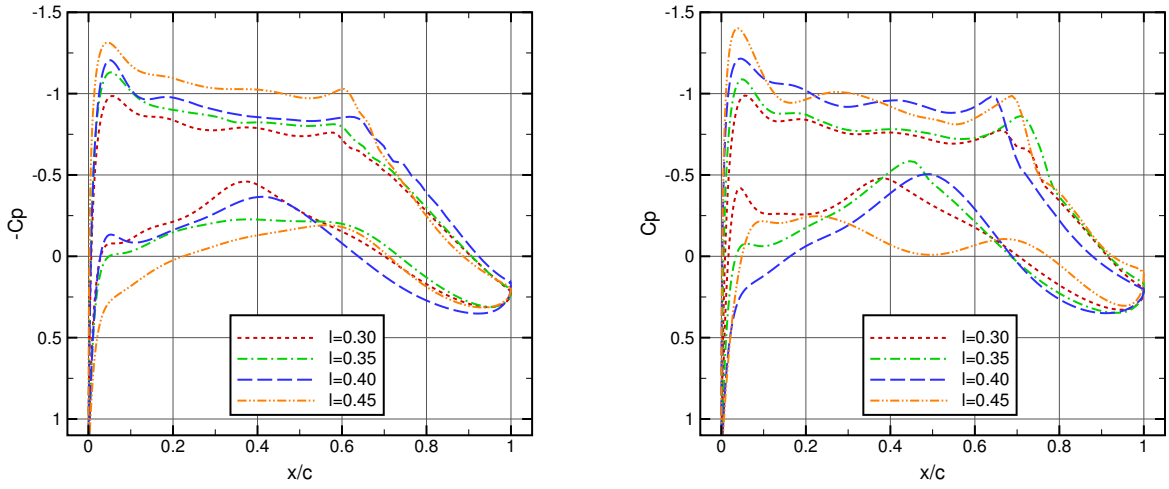

(a) $\kappa = 0.04$ (b) $\kappa = 0.1$

Figure 11: Surface C_P for viscous range optimizations

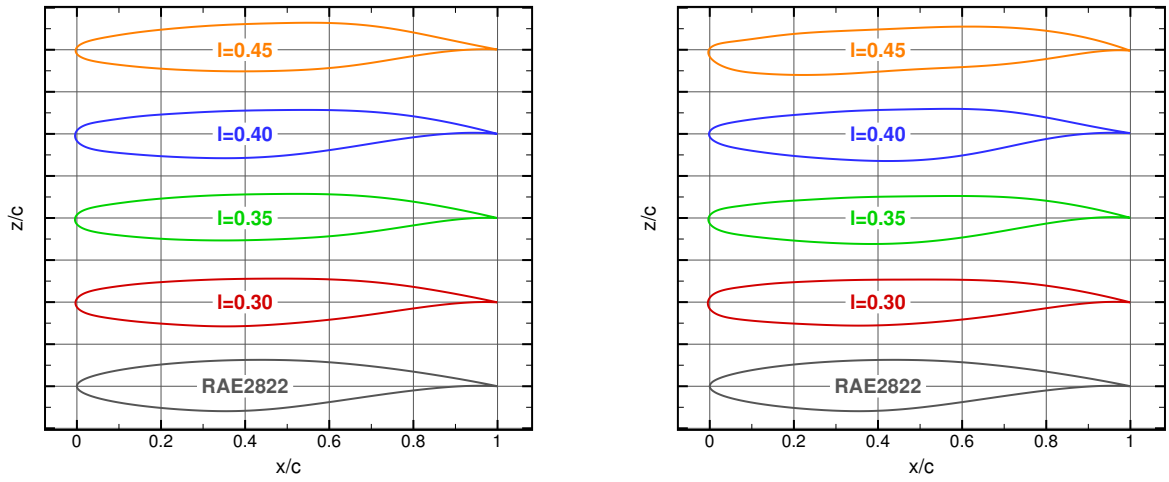

(a) $\kappa = 0.04$ (b) $\kappa = 0.1$

Figure 12: Surface shapes for viscous range optimizations

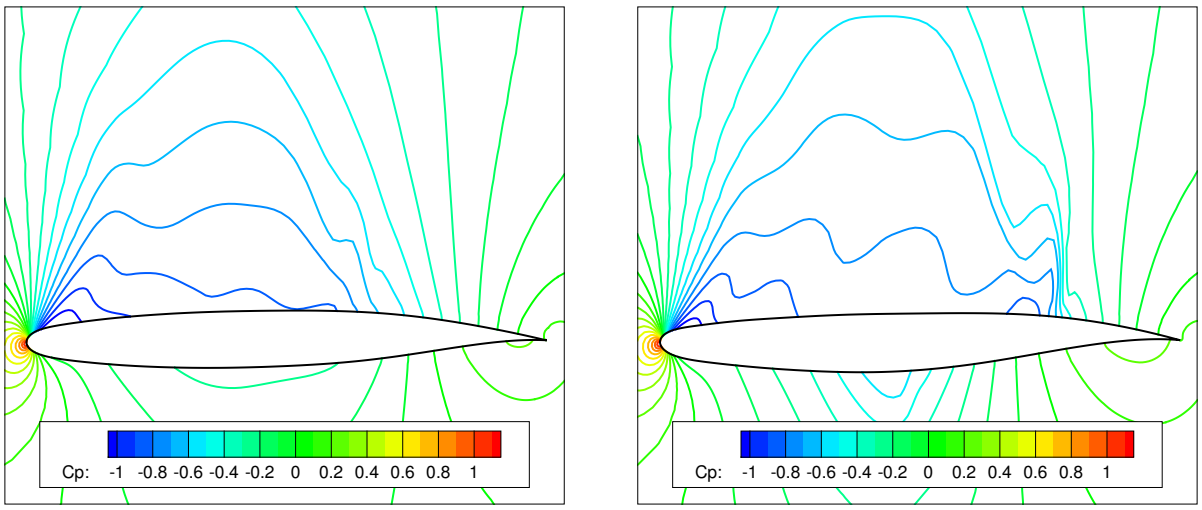

(a) $\kappa = 0.04$ (b) $\kappa = 0.1$

Figure 13: Field C_P lines for range-optimized aerofoils at $l = 0.35$

VI.C. Off-Design Performance

To investigate the off-design performance of the results above, drag-rise curves and performance maps are presented. Figure 14 gives the drag variation with Mach number at a fixed C_L for viscous optimizations. The C_L for each curve is the design C_L, so care has to be taken when comparing the absolute performance of each aerofoil. Furthermore, since C_L is fixed, l is varying and the l values given in the legend are those that the aerofoils were optimized at. The behaviour of the single- and multi-point cases are typical, with a drop in the drag coefficient around the design point and then a drag rise. However, this is also something that is seen in the range optimizations. The lower induced drag factor ($\kappa = 0.04$) produced shock-free solutions, so the local performance improvement is not surprising. However, even the shock solutions (those at $\kappa = 0.1$) show this type of behaviour. It appears that producing shocked optimum solutions does not necessarily lead to less point-like performance, at least when considering drag in isolation.

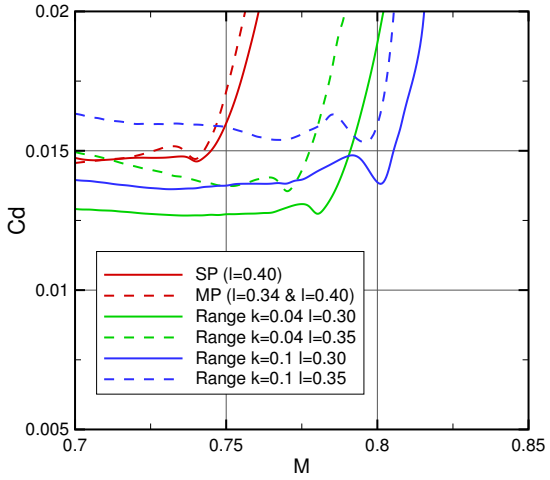

Figure 14: Drag curve at design C_L of optimized aerofoils

Drag is not the only measure of performance, and indeed the optimization problem considered here is range. As such, performance maps are constructed, which give the normalised (by the maximum range) range and are given in figure 15. The 97% contour is also highlighted, the area enclosed by which gives a measure of robustness. This area has been calculated and the results are given in table 7 for all of the viscous results. Clearly, moving to the range optimization has resulted in an overall larger area in the $M - C_L$ space that contains high range performance, hence the range optimizations are more robust to changes in the operating conditions.

It is also observed that the optimum range often does not occur at (or even close to) the final optimized design point. Since the optimum point for the range optimizations must lie on the non-dimensional wing loading constraint, the optimization is somewhat restricted. Since there is a better range that exists at a

Table 7: Area contained within 97% maximum range contour in M-C_L space

Optimization	Integral
RAE2822	4.8×10^{-3}
Single-point	2.8×10^{-3}
Multi-point	3.6×10^{-3}
Range, $\kappa = 0.04$, $l = 0.30$	5.6×10^{-3}
Range, $\kappa = 0.04$, $l = 0.35$	7.2×10^{-3}
Range, $\kappa = 0.04$, $l = 0.40$	7.5×10^{-3}
Range, $\kappa = 0.04$, $l = 0.45$	7.0×10^{-3}
Range, $\kappa = 0.1$, $l = 0.30$	5.0×10^{-3}
Range, $\kappa = 0.1$, $l = 0.35$	5.8×10^{-3}
Range, $\kappa = 0.1$, $l = 0.40$	5.5×10^{-3}
Range, $\kappa = 0.1$, $l = 0.45$	6.7×10^{-3}

different value of l, the question is raised of is there an overall optimum value of l. This is considered in section VI.E.

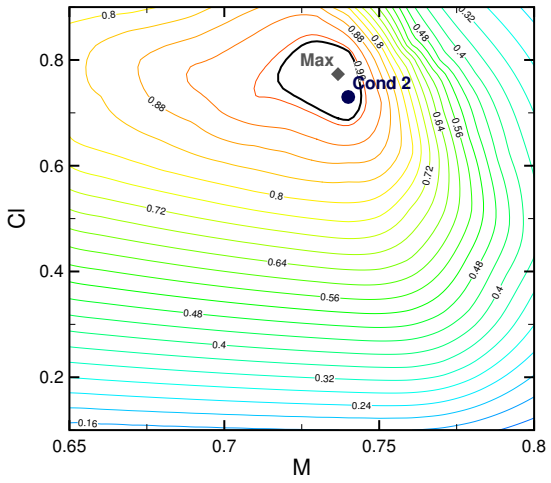

(a) Single-point

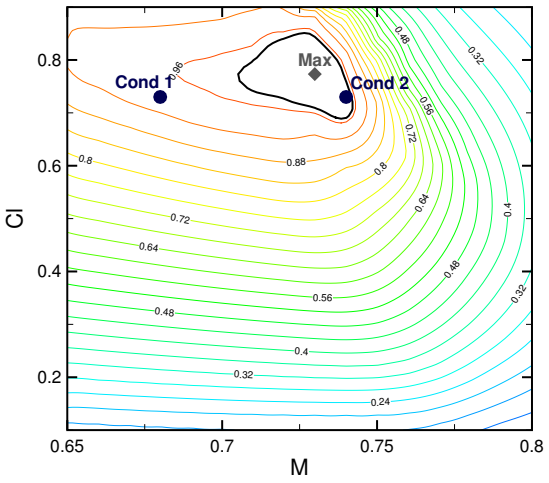

(b) Multi-point

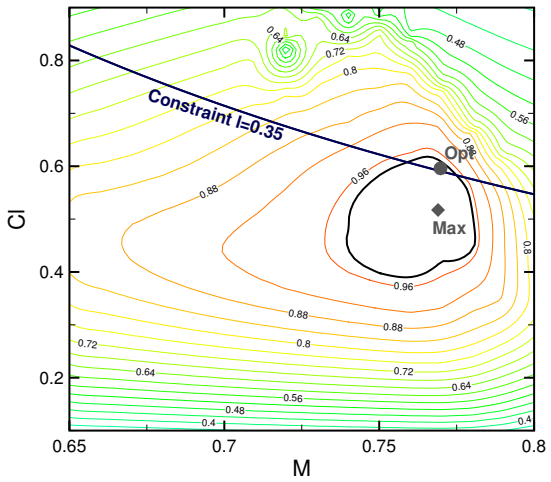

(c) Range ($\kappa = 0.04, l = 0.35$)

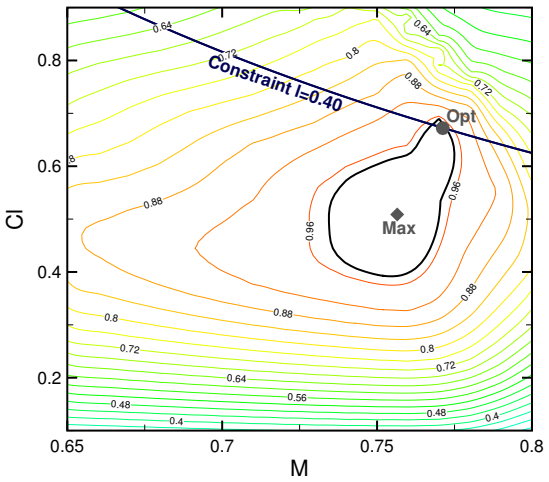

(d) Range ($\kappa = 0.04, l = 0.40$)

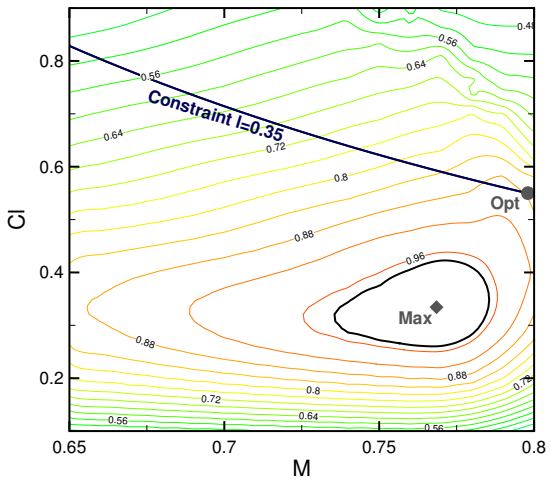

(e) Range ($\kappa = 0.1, l = 0.35$)

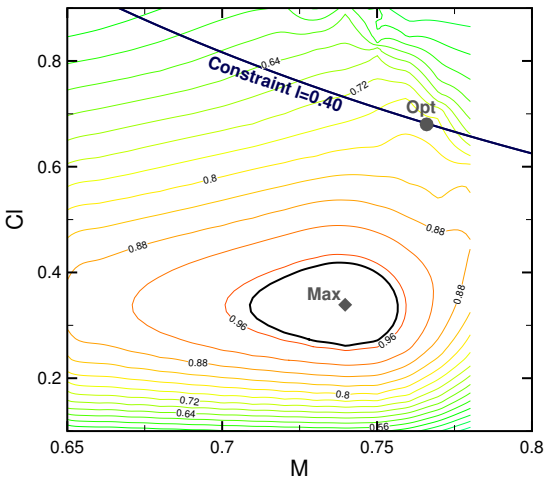

(f) Range ($\kappa = 0.1, l = 0.40$)

Figure 15: M-C_L maps with normalised ML/D contours of optimized aerofoils (97% contour highlighted)

VI.D. Computational Cost

A comparison of the computational cost of the various optimization approaches is given here. When running the FSQP optimizer, the overall cost is driven by the objective evaluation, gradient evaluation and the line search (which requires multiple objective evaluations). Since the gradients are evaluated by a central difference, and this is parallelised, the cost is of the order of two flow solutions (one for each positive and negative perturbation). However, the line search is causal and computed in serial so the number of flow solutions required is unknown *a priori* which can lead to substantial differences in run-times between optimization runs which have approximately the same number of design variables.

Table 8 outlines the cost of the optimizations in terms of number of iterations, number of solver runs and the total wall-time. The convergence histories are given in figure 16. All optimizations were performed on 2.6GHz Intel Sandy Bridge chips. Generally, the range optimizations have a similar total cost to the single-point optimization. However, the high induced drag factor (which leads to shocked results), converges in fewer iterations but longer time than the lower induced drag factor indicating that if the solution is shocked, more serial line search iterations are required to find the optimal strength of the shock.

Table 8: Details of optimization computational cost

		Solver calls		Wall-time (hrs)	
Case	Iterations	Optimization	Sweep	Optimization	Sweep
Single-point	73	2748	500	83	36
Multi-point	83	5732	500	118	36
Range, $\kappa = 0.04$, $l = 0.30$	67	2786	500	87	36
Range, $\kappa = 0.04$, $l = 0.35$	86	3364	500	94	36
Range, $\kappa = 0.04$, $l = 0.40$	94	3656	500	101	36
Range, $\kappa = 0.04$, $l = 0.45$	81	3210	500	92	36
Range, $\kappa = 0.1$, $l = 0.30$	56	2812	500	113	36
Range, $\kappa = 0.1$, $l = 0.35$	39	2370	500	113	36
Range, $\kappa = 0.1$, $l = 0.40$	35	2302	500	116	36
Range, $\kappa = 0.1$, $l = 0.45$	80	3232	500	96	36

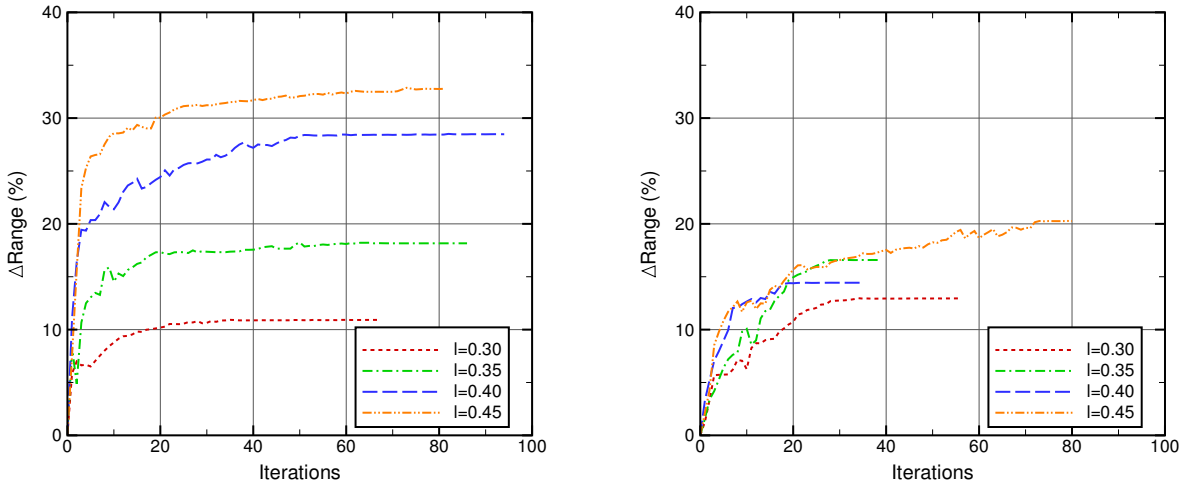

(a) $\kappa = 0.04$ (b) $\kappa = 0.1$

Figure 16: Range optimization convergence histories

VI.E. Optimum Non-Dimensional Wing Loading

The range optimizations presented above all require specification of the required non-dimensional wing loading, as well as the baseline aerofoil (which effectively gives a value for the volume constraint). Also, with the addition of the induced drag penalty, the value of κ needs to be specified. So there exists only the one aerodynamic constraint. Furthermore, as noted above, the performance maps (figure 15) show that a better optimum range in the M-C_L design space is possible if a different non-dimensional wing loading is chosen for that given shape. Hence, for a given volume and induced drag penalty the question exists of what is the optimum range, without the specification of loading. The optimization problem being solved is therefore:

$$\begin{aligned} \underset{\boldsymbol{\alpha},M}{\text{maximise}} \quad & M\frac{C_L}{C_D + \kappa C_L^2} \\ \text{subject to} \quad & V \geq V_{initial} \end{aligned} \tag{31}$$

The final optimization results for $\kappa = 0.04$ and $\kappa = 0.1$ are given in table 9 while the surface pressures and shapes are given in figure 17. The final optimum non-dimensional wing loading values are clearly driven by the value of the induced drag penalty, and this is expected based on the results from figure 15. Adding more induced drag has the effect of pushing the Mach number higher, with a much lower lift coefficient due to this acting to penalise the range. The optimum l values do correlate very well with the the optimum range locations seen in figure 15 e.g. for the range optimized aerofoil at $\kappa = 0.04$ and $l = 0.40$, the optimum range actually occurs at $l = 0.28$, which is very close to the theoretical optimum for $\kappa = 0.04$. However, the surface shapes appear to be remarkably similar for both values of induced drag penalty.

Table 9: Results for viscous range optimizations without specified l

κ	C_L	C_D	C_{D_i}	M	l	ML/D
0.04	0.47	0.0126	0.0088	0.780	0.286	17.1
0.1	0.32	0.0121	0.0101	0.799	0.204	11.4

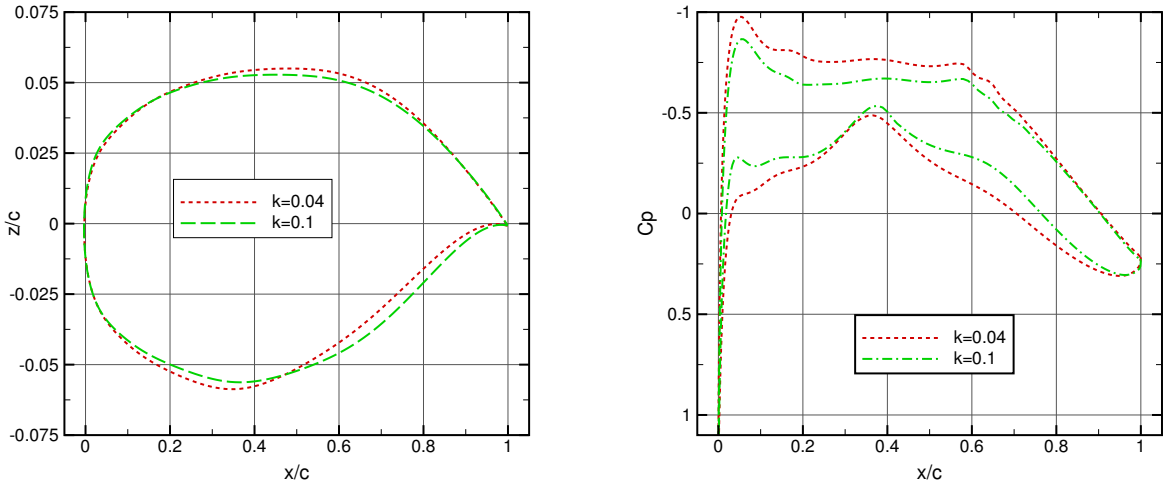

Figure 17: Surface C_P and shapes viscous range optimizations without specified l

VII. Conclusions

A study into the effect of the choice of optimization problem for aerodynamic shape optimization has been presented. As well as single- and multi-point optimizations, a Breguet range problem is considered with the design point (characterised by Mach number and lift coefficient) allowed to vary. A non-dimensional measure of wing loading is therefore a constraint. The study presented has investigated a suitable posing of the transonic aerofoil problem from the point of view of suggesting an optimization problem that has a shocked optimal solution in an attempt to minimise the off-design penalties associated with optimizing at a specific design point. An analytical treatment of the problem has shown that the optimal Mach number for the range optimization is supercritical if the specified lift is over a minimum limit for a given shape.

To consider the effect of optimizing the shape of this problem, transonic inviscid and viscous optimizations have been performed with an induced drag factor added to mimic, more closely, the real trade-offs that exist in aircraft design. It has been shown that a shocked optimal solution can be found when performing range optimization, indicating that this may be a more practical optimization problem than drag minimization that is also more indicative of an industrial design objective. The resulting shocked solutions come about specifically by not fixing the design point, allowing the optimizer to locate a shocked optimum if this is permitted. Since for a fixed design point, the range optimization reduces down to drag minimization, the

resulting optimum design point must be above the boundary at which shock-free solutions are no longer possible.

The overall trend in range optimization is to produce an aerofoil that appears to be of a supercritical family, with high optimal Mach numbers that are high enough to produce shocked solutions, and low trimmed lift coefficients. Any changes to the total loading required are accounted for by having higher lift coefficients, with small reductions in the freestream Mach number indicating that for optimal range, keeping Mach number as high as possible is advantageous.

The off-design performance in drag of shock-free drag minimizations and shocked range optimizations appears to be similar, with the shocked solutions not necessarily leading to more robust performance in drag. However, when range is considered, there is a considerable improvement in the off-design performance, with the overall performance improvements being less restricted to one area of the operating space.

Acknowledgements

The authors kindly acknowledge the support of the Engineering and Physcial Sciences Research Council (EPSRC)-supported University of Bristol EPSRC Doctoral Training Grant. This work was carried out using the computational facilities of the Advanced Computing Research Centre, University of Bristol[d].

References

[1] Hicks, R. M. and Henne, P. A., "Wing Design by Numerical Optimization," *Journal of Aircraft*, Vol. 15, No. 7, 1978, pp. 407–412.
doi:10.2514/6.1977-1247.

[2] Qin, N., Vavalle, A., Le Moigne, A., Laban, M., Hackett, K., and Weinerfelt, P., "Aerodynamic Considerations of Blended Wing Body Aircraft," *Progress in Aerospace Sciences*, Vol. 40, No. 6, 2004, pp. 321–343.
doi:10.1016/j.paerosci.2004.08.001.

[3] Nielsen, E. J., Lee-Rausch, E. M., and Jones, W. T., "Adjoint Based Design of Rotors in a Noninertial Frame," *Journal of Aircraft*, Vol. 47, No. 2, 2010, pp. 638–646.
doi:10.2514/1.46044.

[4] Lyu, Z., Kenway, G. K. W., and Martins, J. R. R. A., "Aerodynamic Shape Optimization Investigations of the Common Research Model Wing Benchmark," *AIAA Journal*, Vol. 53, No. 4, 2015, pp. 968–985.
doi:10.2514/1.J053318.

[d] http://www.bris.ac.uk/acrc/

[5] Choi, S., Lee, K. H., Potsdam, M., and Alonso, J. J., "Helicopter Rotor Design Using a Time-Spectral and Adjoint Based Method," *Journal of Aircraft*, Vol. 51, No. 2, 2014, pp. 412–423. doi:10.2514/1.C031975.

[6] Morris, A. M., Allen, C. B., and Rendall, T. C. S., "CFD-based Optimization of Aerofoils Using Radial Basis Functions for Domain Element Parameterization and Mesh Deformation," *International Journal for Numerical Methods in Fluids*, Vol. 58, No. 8, 2008, pp. 827–860. doi:10.1002/fld.1769.

[7] Allen, C. B. and Rendall, T. C. S., "Computational-Fluid-Dynamics-Based Optimisation of Hovering Rotors Using Radial Basis Functions for Shape Parameterisation and Mesh Deformation," *Optimization and Engineering*, Vol. 14, 2013, pp. 97–118. doi:10.1007/s11081-011-9179-6.

[8] Morawetz, C. S., "On the non-existence of continuous transonic flows past profiles I," *Communications on Pure and Applied Mathematics*, Vol. 9, No. 1, 1956, pp. 45–68. doi:10.1002/cpa.3160090104.

[9] Morawetz, C. S., "On the non-existence of continuous transonic flows past profiles II," *Communications on Pure and Applied Mathematics*, Vol. 10, No. 1, 1957, pp. 107–131. doi:10.1002/cpa.3160100105.

[10] Garabedian, P. R. and Korn, D. G., "Analysis of Transonic Airfoils," *Communications on Pure and Applied Mathematics*, Vol. 24, No. 6, 1971, pp. 841–851. doi:10.1002/cpa.3160240608.

[11] Boerstoel, J., "A Survey of Symmetrical Transonic Potential Flows around Quasi-elliptical Aerofoil Sections," Tech. rep., NLR, 1967, NLR Report TR.T179.

[12] Nieuwland, G., "Transonic Potential Flow around a Family of Quasi-elliptical Aerofoil Sections," Tech. rep., NLR, 1967, NLR Report TR.T172.

[13] Harbeck, M. and Jameson, A., "Exploring the Limits of Transonic Shock-free Airfoil Design," *43rd AIAA Aerospace Sciences Meeting and Exhibit*, Reno, Nevada, 2005, AIAA Paper 2005-1041. doi:10.2514/6.2005-1041.

[14] Carrier, G., Destarac, D., Dumont, A., Meheut, M., Salah El Din, I., Peter, J., Ben Khelil, S., Brezillon, J., and Pestana, M., "Gradient-Based Aerodynamic Optimization with the elsA Software," *52nd AIAA Aerospace Sciences Meeting*, National Harbor, Maryland, 2014, AIAA Paper 2014-0568. doi:10.2514/6.2014-0568.

[15] Bisson, F., Nadarajah, S. K., and Shi-Dong, D., "Adjoint-Based Aerodynamic Optimization Framework," *52nd AIAA Aerospace Sciences Meeting*, National Harbor, Maryland, 2014, AIAA Paper 2014-0412. doi:10.2514/6.2014-0412.

[16] Poole, D. J., Allen, C. B., and Rendall, T. C. S., "Control Point-Based Aerodynamic Shape Optimization Applied to AIAA ADODG Test Cases," *53rd AIAA Aerospace Sciences Meeting*, Kissimmee, Florida, 2015, AIAA Paper 2015-1947. doi:10.2514/6.2015-1947.

[17] LeDoux, S. T., Vassberg, J. C., Young, D. P., Fugal, S., Kamenetskiy, D., Huffman, W. P., Melvin, R. G., and Smith, M. F., "Study Based on the AIAA Aerodynamic Design Optimization Discussion Group Test Cases," *AIAA Journal*, Vol. 53, No. 7, 2015, pp. 1910–1935. doi:10.2514/1.J053535.

[18] Lee, C., Koo, D., Telidetzki, K., Buckley, H. P., Gagnon, H., and Zingg, D. W., "Aerodynamic Shape Optimization of Benchmark Problems Using Jetstream," *53rd AIAA Aerospace Sciences Meeting*, Orlando, Florida, 2015, AIAA Paper 2015-0262. doi:10.2514/6.2015-0262.

[19] Masters, D. A., Taylor, N. J., Rendall, T. C. S., and Allen, C. B., "Multilevel Subdivision Parameterization Scheme for Aerodynamic Shape Optimization," *AIAA Journal*, Vol. 55, No. 10, 2017, pp. 3288–3303. doi:10.2514/1.J055785.

[20] Morawetz, C. S., "On the non-existence of continuous transonic flows past profiles III," *Communications on Pure and Applied Mathematics*, Vol. 11, No. 1, 1958, pp. 129–144. doi:10.1002/cpa.3160110107.

[21] Jameson, A., Vassberg, J. C., and Ou, K., "Further Studies of Airfoils Supporting Non-Unique Solutions in Transonic Flow," *AIAA Journal*, Vol. 50, No. 12, 2012, pp. 2865–2881. doi:10.2514/1.J051713.

[22] Harris, C. D., "NASA Supercritical Airfoils: A Matrix of Family-Related Airfoils," Tech. rep., Langley Research Center, Hampton, Virginia, 1990, NASA Technical Paper 2969.

[23] Epstein, B., Jameson, A., Peigin, S., Roman, D., Harrison, N., and Vassberg, J., "Comparative Study of Three-Dimensional Wing Drag Minimization by Different Optimization Techniques," *Journal of Aircraft*, Vol. 46, No. 2, 2009, pp. 526–541. doi:10.2514/1.38216.

[24] Buckley, H. P., Zhou, B. Y., and Zingg, D. W., "Airfoil Optimization Using Practical Aerodynamic Design Requirements," *Journal of Aircraft*, Vol. 47, No. 5, 2010, pp. 1707–1719.
doi:10.2514/1.C000256.

[25] Meheut, M., Destarac, D., Carrier, G., Anderson, G., Nadarajah, S., Poole, D., Vassberg, J., and Zingg, D., "Gradient-Based Single and Multi-points Aerodynamic Optimizations with the elsA Software," *53rd AIAA Aerospace Sciences Meeting*, Kissimmee, Florida, 2015, AIAA Paper 2015-0263.
doi:10.2514/6.2015-0263.

[26] Kenway, G. K. W. and Martins, J. R. R. A., "Multipoint Aerodynamic Shape Optimization Investigations of the Common Research Model Wing," *AIAA Journal*, Vol. 54, No. 1, 2016, pp. 113–128.
doi:10.2514/1.J054154.

[27] Gallard, F., Mohammadi, B., Montagnac, M., and Meaux, M., "An Adaptive Multipoint Formulation for Robust Parametric Optimization," *Journal of Optimization Theory and Applications*, Vol. 167, No. 2, 2015, pp. 693–715.
doi:10.1007/s10957-014-0595-6.

[28] Zingg, D. W. and Elias, S., "Aerodynamic Optimization Under a Range of Operating Conditions," *AIAA Journal*, Vol. 44, No. 11, 2006, pp. 2787–2792.
doi:10.2514/1.23658.

[29] Liem, R. P., Kenway, G. K. W., and Martins, J. R. R. A., "Multimission Aircraft Fuel-Burn Minimization via Multipoint Aerostructural Optimization," *AIAA Journal*, Vol. 53, No. 1, 2015, pp. 104–122.
doi:10.2514/1.J052940.

[30] Buckley, H. P. and Zingg, D. W., "Approach to Aerodynamic Design Through Numerical Optimization," *AIAA Journal*, Vol. 51, No. 8, 2013, pp. 1972–1981.
doi:10.2514/1.J052268.

[31] Liem, R. P., Martins, J. R. R. A., and Kenway, G. K. W., "Expected drag minimization for aerodynamic design optimization based on aircraft operational data," *Aerospace Science and Technology*, Vol. 63, 2017, pp. 344–362.
doi:10.1016/j.ast.2017.01.006.

[32] Drela, M., "Pros and Cons of Airfoil Optimization," in Caughey, D. and Hafez, M., eds., "Frontiers of Computational Fluid Dynamics," World Scientific, pp. 363–381, 1998.
doi:10.1142/9789812815774_0019.

[33] Li, W., Huyse, L. W., and Padula, S., "Robust airfoil optimization to achieve drag reduction over a range of Mach numbers," *Structural and Multidisciplinary Optimization*, Vol. 24, No. 1, 2002, pp. 38–50. doi:10.1007/s00158-002-0212-4.

[34] Doherty, J. J., "Transonic Airfoil Study Using Sonic Plateau, Optimization and Off-Design Performance Maps," *35th AIAA Applied Aerodynamics Conference*, Denver, Colorado, 2017, AIAA Paper 2017-3056. doi:10.2514/6.2017-3056.

[35] Mair, W. A. and Birdsall, D. L., *Aircraft Performance*, Cambridge University Press, 1992.

[36] Hanke, C. R. and Nordwall, D. R., "The Simulation of a Jumbo Jet Transport Aircraft. Volume 2: Modeling Data," Tech. rep., NASA, 1970, NASA-CR-114494.

[37] Iuliano, E., "Global optimization of benchmark aerodynamic cases using physics-based surrogate models," *Aerospace Science and Technology*, Vol. 67, 2017, pp. 273–286. doi:10.1016/j.ast.2017.04.013.

[38] Poole, D. J., Allen, C. B., and Rendall, T. C. S., "Metric-Based Mathematical Derivation of Efficient Airfoil Design Variables," *AIAA Journal*, Vol. 53, No. 5, 2015, pp. 1349–1361. doi:10.2514/1.J053427.

[39] Eckart, C. and Young, G., "The Approximation of One Matrix by Another of Lower Rank," *Psychometrika*, Vol. 1, No. 3, 1936, pp. 211–218. doi:10.1007/BF02288367.

[40] Masters, D. A., Taylor, N. J., Rendall, T. C. S., Allen, C. B., and Poole, D. J., "Geometric Comparison of Aerofoil Shape Parameterization Methods," *AIAA Journal*, Vol. 55, No. 5, 2017, pp. 1575–1589. doi:10.2514/1.J054943.

[41] Poole, D. J., Allen, C. B., and Rendall, T. C. S., "High-fidelity aerodynamic shape optimization using efficient orthogonal modal design variables with a constrained global optimizer," *Computers & Fluids*, Vol. 143, 2017, pp. 1–15. doi:10.1016/j.compfluid.2016.11.002.

[42] Morris, A. M., Allen, C. B., and Rendall, T. C. S., "Domain-Element Method for Aerodynamic Shape Optimization Applied to a Modern Transport Wing," *AIAA Journal*, Vol. 47, No. 7, 2009, pp. 1647–1659. doi:10.2514/1.39382.

[43] Rendall, T. C. S. and Allen, C. B., "Unified Fluid-Structure Interpolation and Mesh Motion Using Radial Basis Functions," *International Journal for Numerical Methods in Engineering*, Vol. 74, No. 10, 2008, pp.

1519–1559.
doi:10.1002/nme.2219.

[44] Rendall, T. C. S. and Allen, C. B., "Efficient Mesh Motion Using Radial Basis Functions with Data Reduction Algorithms," *Journal of Computational Physics*, Vol. 228, No. 17, 2009, pp. 6231–6249.
doi:10.1016/j.jcp.2009.05.013,.

[45] Kennedy, J. and Eberhart, R., "Particle Swarm Optimization," *1995 IEEE International Conference on Neural Networks*, Perth, Australia, 1995.
doi:10.1109/ICNN.1995.488968.

[46] Rashedi, E., Nezamabadi-pour, H., and Saryazdi, S., "GSA: A Gravitational Search Algorithm," *Information Sciences*, Vol. 179, 2009, pp. 2232–2248.
doi:10.1016/j.ins.2009.03.004.

[47] Poole, D. J., Allen, C. B., and Rendall, T. C. S., "A Generic Framework for Handling Constraints with Agent-Based Optimization Algorithms and Application to Aerodynamic Design," *Optimization and Engineering*, Vol. 18, No. 3, 2017, pp. 659–691.
doi:10.1007/s11081-016-9343-0.

[48] Poole, D. J., Allen, C. B., and Rendall, T. C. S., "Global Optimization of Wing Aerodynamic Optimization Case Exhibiting Multimodality," *Journal of Aircraft*, Vol. 0, 2018, p. 0, In print.

[49] Zhou, J. L., Tits, A. L., and Lawrence, C. T., "Users Guide for FSQP Version 3.7 : A Fortran Code for Solving Optimization Programs, Possibly Minimax, with General Inequality Constraints and Linear Equality Constraints, Generating Feasible Iterates," Tech. rep., Institute for Systems Research, University of Maryland, 1997, SRC-TR-92-107r5.

[50] Mayne, D. Q. and Polack, E., "A surperlinearly convergent algorithm for constrained optimization problems," *Mathematical Programming Studies*, Vol. 4, 1982, pp. 45–61.
doi:10.1007/BFb0120947.

[51] Grippo, L., Lampariello, F., and Lucidi, S., "A Nonmonotone Line Search Technique for Newton's Method," *SIAM Journal on Numerical Analysis*, Vol. 23, No. 4, 1986, pp. 707–716.
doi:10.1137/0723046.

[52] Panier, E. R. and Tits, A. L., "Avoiding the Maratos Effect by Means of a Nonmonotone Line Search I. General Constrained Problems," *SIAM Journal on Numerical Analysis*, Vol. 28, No. 4, 1991, pp. 1183–1195.
doi:10.1137/0728063.

[53] Bonnans, J. F., Panier, E. R., Tits, A. L., and Zhou, J. L., "Avoiding the Maratos Effect by Means of a Nonmonotone Line Search II. Inequality Constrained Problems–Feasible Iterates," *SIAM Journal on Numerical Analysis*, Vol. 29, No. 4, 1992, pp. 1187–1202.
doi:10.1137/0729072.

[54] Zhou, J. L. and Tits, A. L., "Nonmonotone Line Search for Minimax Problems," *Journal of Optimization Theory and Applications*, Vol. 76, No. 3, 1993, pp. 455–476.
doi:10.1023/A:1020896407415.

[55] van Leer, B., "Flux-vector splitting for the Euler equations," *Eighth International Conference on Numerical Methods in Fluid Dynamics*, Lecture Notes in Physics, 1982, pp. 507–512.
doi:10.1007/3-540-11948-5_66.

[56] Spalart, P. R. and Allmaras, S. R., "A One-Equation Turbulence Model for Aerodynamic Flows," *Recherche Aérospatiale*, Vol. 1, 1994, pp. 5–21.

[57] Allmaras, S. R., Johnson, F. T., and Spalart, P. R., "Modifications and Clarifications for the Implementation of the Spalart-Allmaras Turbulence Model," *Seventh International Conference on Computational Fluid Dynamics (ICCFD7)*, Big Island, Hawaii, 2012, Paper ICCFD7-1902.

[58] Allen, C. B., "Multigrid Convergence of Inviscid Fixed- and Rotary-Wing Flows," *International Journal for Numerical Methods in Fluids*, Vol. 39, No. 2, 2002, pp. 121–140.
doi:10.1002/fld.282.

[59] Allen, C. B., "Towards Automatic Structured Multiblock Mesh Generation using Improved Transfinite Interpolation," *International Journal for Numerical Methods in Engineering*, Vol. 74, No. 5, 2008, pp. 697–733.
doi:10.1002/nme.2170.

[60] Jameson, A., Vassberg, J. C., and Shankaran, S., "Aerodynamic-Structural Design Studies of Low-Sweep Transonic Wings," *Journal of Aircraft*, Vol. 47, No. 2, 2010, pp. 505–514.
doi:10.2514/1.42775.

[61] Lock, C. N. H., "The Ideal Drag Due to a Shock Wave Parts I and II," Tech. rep., Aeronautical Research Council, 1951, ARC report 2512.

[62] Chernukhin, O. and Zingg, D. W., "Multimodality and Global Optimization in Aerodynamic Design," *AIAA Journal*, Vol. 51, No. 6, 2013, pp. 1342–1354.
doi:10.2514/1.J051835.